Kondo effect and its destruction in hetero-bilayer transition metal dichalcogenides

Fang Xie,^{1,2,*} Lei Chen,¹ and Qimiao Si¹

¹Department of Physics & Astronomy, Rice Center for Quantum Materials, Rice University, Houston, Texas 77005, USA

²Rice Academy of Fellows, Rice University, Houston, Texas 77005, USA

(Dated: February 29, 2024)

Moiré structures, along with line-graph-based d-electron systems, represent a setting to realize flat bands. One form of the associated strong correlation physics is the Kondo effect. Here, we address the recently observed Kondo-driven heavy fermion state and its destruction in AB-stacked hetero-bilayer transition metal dichalcogenides, which can be controlled by the gate voltages. By studying an effective interacting Hamiltonian using the slave spin approach, we obtained a phase diagram with the total filling factor and the displacement field strength as the tunable parameters. In an extended range of the tunable displacement field, our numerical results show that the relative filling of the d orbital, which is associated with the highest moiré band from the MoTe₂ layer, is enforced to be $\nu_d \approx 1$ by the interaction. This agrees with the experimental observation. We also argue that the observed high coherence temperature scale could be explained by the non-negligible bandwidth of the d orbital. Our results set the stage to address the amplified quantum fluctuations that the Kondo effect may produce in these structures and new regimes that the systems open up for Kondo-destruction quantum criticality.

I. INTRODUCTION

Moiré structures provide a setting to study strong correlation physics. One of the first realized moiré structures is magic-angle twisted bilayer graphene, in which multiple strongly correlated phases have been observed in experiments [1, 2]. Multilayers of transition metal dichalcogenide (TMDC) represent another type of moiré structure to study correlation physics. Pertinent to the TMDC moiré structure are a variety of strongly correlated phenomena, such as the correlated Chern insulator, the fractional Chern insulator, the Mott insulator, Wigner crystals, and the Kondo effect [3–27].

In these structures, the moiré energy bands near the Fermi level are typically narrow. Therefore, the kinetic energy is reduced and the correlation effects are proportionally enhanced. This type of behavior is also expected in other materials platforms, such as d-electron-based materials on kagome and other line-graph lattices with geometry-induced flat bands [28–30]. There has been a growing realization that these classes of systems can be described in terms of a Kondo lattice and the associated heavy fermion behavior, as arising in moiré structures based on TMDC [3–7] and graphene [31–41], and in geometry-induced flat-band materials [42–44]. As such, these systems represent new platforms for emulating Kondo-driven correlation physics [45–49].

Here, we show that the AB-stacked MoTe₂/WSe₂ hetero-bilayer realizes a new correlation regime for both the Kondo effect and its destruction. To put our work into perspective, we now describe our specific motivations and provide a brief summary of the main points of our findings.

A. AB-stacked MoTe₂/WSe₂ hetero-bilayer

In AB-stacked MoTe₂/WSe₂ hetero-bilayer moiré structure, the two monolayers with lattice constants mismatch are stacked in opposite directions. Moiré bands near the Fermi level from both layers form localized Wannier states sitting on hexagonal moiré superlattice sites [16, 23] with different bandwidths, which allows a tight-binding description. More precisely, the moiré band which predominately comes from the MoTe₂ layer has a smaller bandwidth than the other moiré band from the WSe₂ layer. In the following, we will denote the Wannier orbital that predominately originates from the $MoTe_2$ layer as d orbital, and the orbital originating from the WSe_2 layer as c orbital. Inter-orbital tunneling is strongly suppressed due to the spin-valley locking mechanism in TMDC materials [16] and the opposite stacking directions. The inter-orbital tunneling is expected to be chiral due to the bilayer stacking [7]. Because of the small bandwidths in moiré structures, the repulsive Coulomb interaction in the c and d orbitals is not negligible. Therefore, an extended two-orbital Hubbard model will be a reasonable minimum model.

In transport experiments, the total electron filling factor and the displacement field perpendicular to the sample plane can be controlled directly by tuning the gate voltages. Since the c and d orbitals come from two different layers, the perpendicular displacement field induces a potential difference between these two orbitals, and thus, the electron fillings in the two individual orbitals can be controlled indirectly.

In this system, a heavy Fermi liquid state has been observed in an extended range of displacement field strengths [3] (see Fig. 11 in App. F). Quite noticeably, the coherence temperature controlling the crossover between the high-temperature incoherent scattering regime and the low-temperature Fermi liquid regime is very high: $T_{\rm coh} \approx 20 \sim 40\,{\rm K}$ (called T^* in Ref. [3]). A sufficiently

^{*} fx7@rice.edu

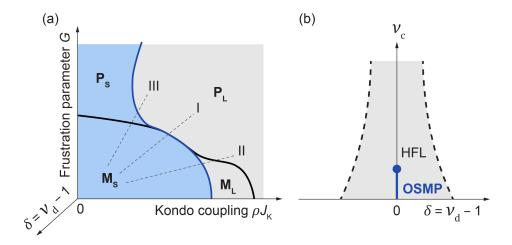


FIG. 1. (a) The global schematic phase diagram of the Kondo lattice. Vertical axis G stands for the frustration strength, and horizontal axis ρJ_K describes the Kondo coupling. The three dashed lines represent possible quantum phase transition sequences between the Kondo-destroyed phases (light blue region: M_S , magnetic ordered small Fermi surface; or P_S , paramagnetic small Fermi surface) and the heavy Fermi liquid states (gray region: P_L , paramagnetic large Fermi surface; or M_L , magnetic ordered large Fermi surface). The third axis, which measures the deviation of the d orbital filling from unity $\delta = \nu_d - 1$, is a new axis that becomes readily tunable in moiré heavy fermion systems. (b) Schematic phase diagram of the two-orbital extended Hubbard model in the parameter space of d orbital filling factor $\delta = \nu_d - 1$ and c orbital filling factor ν_c . Here HFL stands for heavy Fermi liquid and OSMP (blue line) stands for orbital-selective Mott phase, in which the Kondo screening is destructed and local spin moments can form.

large magnetic field suppresses this heavy Fermi liquid state, as can be understood by the magnetic-field-induced suppression of the Kondo effect [45]. Very recently, a magnetic ordered phase with destructed Kondo screening was also observed by reducing the filling of the c orbital [4]. These recent experimental discoveries indicate that the AB-stacked MoTe₂/WSe₂ hetero-bilayer is a promising candidate for studying Kondo-driven correlation physics.

B. Kondo effect

The Kondo effect underlies the extremely strong correlations of heavy fermion metals. Historically, heavy fermion metals have provided a canonical system for the understanding of Fermi liquid phases with large renormalization factors [45].

When the two bandwidths strongly differ, the narrower band can act as local moments while the wider band remains it inerant. This regime develops in frustrated d-electron systems, when the near-Fermi-energy flat bands and their topological nature are taken into account [42–44], forming a new correlation regime in which the local Coulomb repulsion U is in between the two bandwidths.

However, the bandwidths and the interaction of the AB-stacked MoTe₂/WSe₂ hetero-bilayer do not seem to fall in this regime. The ratio of the two bandwidths is only about 2 and the interaction strength is not small in the WSe₂ layer (see details below). One of the objec-

tives of our work is to assess the correlation regime of the two-orbital Hubbard model. We anchor our consideration in terms of the coherent temperature, which has been experimentally measured, by exploring the implication of the aforementioned magnitudes of the bandwidths and interaction strength and the inter-layer hybridization strength. The observed coherent temperature is incompatible with any estimate in the local-moment-based Kondo regime. Using a saddle-point treatment of the microscopic Hamiltonian, we argue that it instead implicates a more general correlation regime.

C. Kondo destruction

In the modern period of the heavy fermion field, heavy fermion metals have become active frontiers for the exploration of metallic quantum criticality [46–49] (as well as strongly correlated metallic topology [50–52]). A catalyst for extensive theoretical understanding and experimental studies has been the notion of Kondo destruction. The Kondo destruction theory was advanced in a study of the dynamical competition between the Kondo and Ruderman–Kittel–Kasuya–Yosida (RKKY) interactions in Kondo lattice models [53], and was subsequently discussed [54] and studied [55] based on alternative approaches. Experimental evidence has come from a variety of heavy fermion metals [56–61]. In the Kondo regime, the RKKY interaction favors a ground state with the quantum magnetism of the local moments. This process

induces a dynamical competition against the formation of a Kondo singlet. The ensuing destruction of the Kondo effect leads to amplified quantum fluctuations. Because the nature of the ground state associated with the quantum magnetism itself can vary from genuine long-range magnetic order to being disordered (without symmetry breaking), the competition leads to a global phase diagram, as summarized in the main plane of Fig. 1(a) [62– 65. The Kondo lattice undergoes a transition from the heavy Fermi liquid state with a large Fermi surface (P_L or M_L , labeled by gray), which incorporates the local moments into the Fermi volume, into a small Fermi surface state that does not count the local moments in the Fermi volume (P_S or M_S , labeled by blue). Most extensive studies have focused on the case when the "M" phase corresponds to an antiferromagnetic order, where the strength of frustration G affects the degree of the order. The case of ferromagnetic order has also been considered [66, 67], though the role of frustration becomes uncertain. The salient properties associated with the Kondo destruction QCP also includes a dynamical "Planckian" ($\hbar\omega/k_{\rm B}T$) scaling, the associated linear-in-T relaxation rate, and loss of the quasiparticles at the QCP [47–49, 68].

For the AB-stacked MoTe₂/WSe₂ hetero-bilayer, the extended correlation regime that has been implicated by considerations of the coherent temperature scale, as summarized in the previous subsection, also raises the question of the type of phase transition that can take place. In this work, we address the issue within the saddle-point analysis in the non-magnetic sector. Our analysis does find a Kondo destruction, starting from a regime of heavy fermion phase that is implicated by the magnitude of the observed coherence temperature. Our results are qualitatively summarized in Fig. 1(b). Our findings set the stage for further dynamical analyses of the model to explore the realization of other salient properties of the Kondo destruction. We discuss the issue further in Sec. V.

D. A new axis in the phase diagram

An important advantage of moiré structures is that a gate voltage readily tunes the electron density. The variation, however, is the total density ν . We can express ν as the sum of the electron density for the MoTe₂ layer, ν_d , and that for the WSe₂ layer, ν_c . Thus, a new axis arises, namely the deviation of ν_d from half-filling. This is illustrated as a new axis of $\delta = \nu_d - 1$ in Fig. 1(a) for the global phase diagram. More specifically, we illustrated the result of our saddle point calculations in the generalized phase diagram Fig. 1(b), where the vertical axis represents a cut in the $\delta = 0$ plane of the global phase diagram illustrated in Fig. 1(a). We stress two particular aspects of Fig. 1(b). First, $\delta = 0$ develops for a range of the total density ν ; this pinning of the d-electron density to half-filling results from strong correlations. In this pinned range, the transition point

between the heavy Fermi liquid and the orbital-selective Mott phase (OSMP) along the line captures an overall transition across the blue line in the global phase diagram of Fig. 1(a). Second, the heavy Fermi liquid state can still exist if the d orbital is slightly doped from unity (i.e., when $|\delta| \ll 1$). If the d orbital filling factor ν_d is tuned significantly away from unity, one can anticipate a crossover out of the heavy Fermi liquid, resulting in a reduction in the effective mass of the d orbital.

More specifically, we use a saddle-point approach based on the U(1) slave spin representation [69] to study the effective model for the TMDC hetero-bilayer with the total electron density $\nu = \nu_c + \nu_d$ and the displacement field potential ε_D as tuning parameters. We demonstrate that the stripe-shaped heavy Fermi liquid region in this two-parameter space observed in experiment [3, 4] can be well captured by our calculation. The transition between the heavy Fermi liquid state and OSMP, which is associated with the reduction of the conduction electron density, is also observed in the numerical results shown in Fig. 5(d).

This article is organized as follows. In Sec. II, we briefly introduce the tight-binding and interacting Hamiltonian and the definition of the tunable parameters that will be used later. Then we present the general and numerical results about the heavy Fermi liquid in Sec. III, and about the orbital-selective Mott phase transition and Kondo destruction in Sec. IV. Finally we discuss results in Sec. V, and we summarize our findings in Sec. VI.

II. MODEL

In this section, we briefly introduce the model Hamiltonian for the AB-stacked bilayer MoTe₂/WSe₂ system. We start from the effective tight-binding model on a hexagonal lattice, and then present an interacting Hamiltonian based on this lattice model. A detailed discussion about the Hamiltonian can be found in App. A.

A. Tight-binding model

Monolayer TMDC materials in the 2H structural phase are known to have strong spin-orbital coupling, which leads to spin-valley locking [70, 71]. As depicted in Fig. 2(a), the hole pocket near valley $\mathcal K$ exclusively has a spin- \uparrow band, whereas the pocket near $\mathcal K'$ only contains a spin- \downarrow band.

In hetero-bilayer TMDC systems, the difference in unit cell size results in a lattice mismatch that can cause the formation of a moiré superlattice at zero-angle twisting. As a result, the size of the moiré Brillouin zone is determined by the difference between the Brillouin zones of the two monolayers, as illustrated in Fig. 2(b). In valley \mathcal{K} , the top band edge of the MoTe₂/WSe₂ band will be centered around the K/K' point in the moiré Brillouin zone, respectively. Since the two layers are AB-stacked, the hole bands from the two layers in the same valley

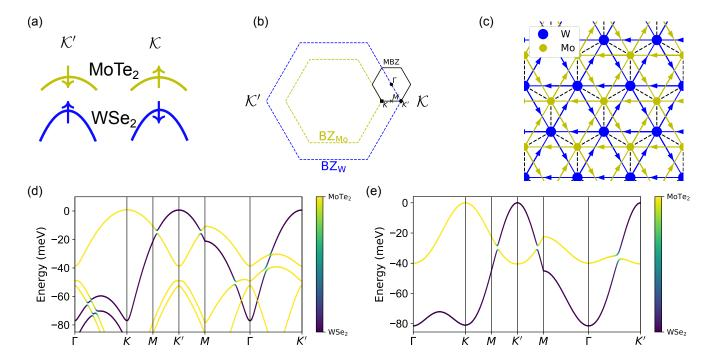


FIG. 2. (a) The spin-valley locking of monolayer TMDC materials. Here we use $\mathcal{K}, \mathcal{K}'$ to represent the two valleys of the monolayer Brillouin zones. Since the two layers are stacked oppositely, the hole pockets in the same valley will have opposite spins. (b) The relationship between the monolayer Brillouin zones (yellow and blue hexagons with dashed lines) and the moiré Brillouin zone (black hexagon). (c) Effective tight-binding model of a single valley on a hexagonal lattice. Intra-layer hoppings in valley τ along the direction of the arrows have a phase factor $e^{\tau i \frac{2\pi}{3}}$ in the WSe₂ layer, or $e^{-\tau i \frac{2\pi}{3}}$ in the MoTe₂ layer. Inter-layer hoppings are shown by black dashed lines. Because of the spin-valley locking, these inter-layer hoppings flip the electron spin. (d) The single valley band structure of the continuum model. The inter-layer hoppings open a small gap along M-K'-M lines, and the highest moiré band above this hybridization gap carries non-zero Chern number $\mathcal{C} = \pm 1$. (e) The tight-binding model band structure with $t_c = 9$ meV, $t_d = 4.5$ meV, and $t_{cd} = 1.5$ meV. In this figure, the interlayer potential ε_D is chosen such that the top band edges of the two bands are at the same energy. The tight-binding model is able to capture the key features of the highest moiré bands qualitatively.

will carry opposite spin quantum numbers. As a consequence, the inter-layer hoppings only consist of spin-flipping terms, which are anticipated to be weak.

Similar to the Bistritzer-MacDonald model [72] for twisted bilayer graphene, a single valley continuum model can also be derived for the AB-stacked TMDC [16, 23]. The band structure of the continuum model can be found in Fig. 2(d). Since the hole pockets in the two types of monolayers have different effective mass, the highest moiré bands will also exhibit different bandwidths: the moiré band from MoTe₂ has a bandwidth $D_{\text{Mo}} \sim 40 \text{ meV}$, while the other layer has $D_{\text{W}} \sim 80 \text{ meV}$.

Although the continuum model is more accurate, it is challenging to study compared to a simplified tight-binding model. By analyzing the symmetry of the continuum model [73], a tight-binding model, which is able to capture the major low energy features of this system, can be constructed from the continuum model [16, 19, 20, 23]. The charge centers of the orbitals from each layer can form triangular moiré superlattices, and they are located at two distinct hexagonal sites belonging to two different Wyckoff positions, which are represented by yellow and blue markers in Fig. 2(c). Therefore, the tight-binding model can be written on the hexagonal lattice,

with two orbitals per unit cell. We use $c_{i\tau}^{\dagger}/d_{i\tau}^{\dagger}$ to represent the fermionic creation operator of the orbital from the WSe₂/MoTe₂ layer and valley τ at superlattice site i. Here $\tau=\pm$ represent the single-layer valley indices, which correspond to \mathcal{K} and \mathcal{K}' , respectively. One can write down the following tight-binding Hamiltonian with four bands [19, 20]:

$$H_{0} = \sum_{\langle\langle ij\rangle\rangle,\tau} t_{c} e^{\tau i \phi_{ij}^{c}} c_{i\tau}^{\dagger} c_{j\tau} + \sum_{\langle\langle ij\rangle\rangle,\tau} t_{d} e^{\tau i \phi_{ij}^{d}} d_{i\tau}^{\dagger} d_{j\tau}$$
$$+ \sum_{\langle\langle ij\rangle,\tau} \left(t_{cd} c_{i\tau}^{\dagger} d_{j\tau} + \text{h.c.} \right) + \frac{\varepsilon_{D}}{2} \sum_{i\tau} \left(c_{i\tau}^{\dagger} c_{i\tau} - d_{i\tau}^{\dagger} d_{i\tau} \right) . \tag{1}$$

Here $\langle\langle ij\rangle\rangle$ denotes the next-nearest neighbor sites, which are always intra-layer terms, while $\langle ij\rangle$ represents the nearest neighbor sites, exclusively connecting sites from different layers. The phase factors associated with the intra-layer hoppings are chosen to be $\phi_{ij}^c = 2\pi/3$ and $\phi_{ij}^d = -2\pi/3$ along the arrows in Fig. 2(c). These hopping phases will result in the top band edges of the MoTe₂/WSe₂ bands being located at the K/K' points in valley $\tau = +$. As shown by the dashed lines in Fig. 2(c),

the inter-layer hoppings are along the nearest neighbor directions instead of on-site. This leads to a chiral signature with the form of $k_x \pm ik_y$ near K and K' in the hybridization function, which is different from the momentum-independent hybridization in standard Anderson models, as has been studied in Ref. [7]. ε_D represents the potential difference between the two layers induced by the displacement field.

By fitting the tight-binding model with the dispersion of the continuum model, these parameters can be set to the following values:

$$t_c \approx 9 \text{ meV}$$
,
 $t_d \approx 4.5 \text{ meV}$,
 $t_{cd} \approx 1.5 \text{ meV}$. (2)

The dispersion of the tight-binding model is also shown in Fig. 2(e). Qualitative features of the highest moiré bands in the continuum model can be well-captured by this simple tight-binding model. Therefore, we will use these tight-binding parameters throughout this manuscript unless otherwise stated.

B. Interacting Hamiltonian

Kondo-driven physics is usually modeled by the Anderson lattice Hamiltonian. However, it is crucial to assess whether the AB-stacked TMDC hetero-bilayer can be well described by the standard Anderson lattice Hamiltonian. Indeed, a few factors beyond the Anderson lattice model need to be considered. The bandwidth ratio between the two bands from the MoTe₂ and WSe₂ layers is not very small: $D_{\rm Mo}/D_{\rm W}\sim 0.5$. Both $D_{\rm W}$ and D_{Mo} might be comparable to the strength of the on-site interaction in the hetero-bilayer TMDC moiré material. Hence, (i) the dispersion of the d bands is not negligible, and (ii) the interaction in the conduction band has to be considered. We also note that (iii) the non-local interaction terms might not be negligible when compared with the on-site interaction [15, 21]. As indicated by previous studies, these non-local interaction terms are able to affect the quasiparticle weight Z [74], and contribute to the stabilization of inter-valley excitonic order, leading to a quantum anomalous Hall effect in this system [20, 75]. Therefore, we choose the multi-orbital extended Hubbard Hamiltonian as our minimum model, which is more general than the standard Anderson lattice Hamiltonian, though in the latter case the effect of a correlated conduction band has been discussed [76]. The interacting

Hamiltonian can be written the following form:

$$H_{I} = \frac{U}{2} \sum_{i,\alpha=c,d} (n_{i\alpha+} + n_{i\alpha-} - 1)^{2}$$

$$+ V \sum_{\langle ij\rangle,\tau\tau'} \left(n_{ic\tau} - \frac{1}{2} \right) \left(n_{jd\tau'} - \frac{1}{2} \right)$$

$$+ V' \sum_{\langle\langle ij\rangle\rangle,\alpha\tau\tau'} \left(n_{i\alpha\tau} - \frac{1}{2} \right) \left(n_{j\alpha\tau'} - \frac{1}{2} \right) , \quad (3)$$

in which $n_{i\alpha\tau} = \alpha_{i\tau}^{\dagger} \alpha_{i\tau}$, $\alpha = c$ or d is the electron density operator. Here we use U to represent the onsite interaction, V to represent the inter-orbital [nearest-neighbor (NN)] interaction, and V' to represent the next-nearest-neighbor (NNN) interaction. The interaction strength in the lattice model can be estimated from the Wannier functions of the orbitals, and the on-site interaction U is indeed comparable to the bandwidth of the wide band $D_{\rm W}$.

III. HEAVY FERMI LIQUID

Based on experimental observations, the heavy Fermi liquid behavior is predominantly observed within a stripe-like region in the (ε_D, ν) phase diagram [3] when the total hole filling factor is in the interval $1 < \nu < 2$. Hence, we first choose the strength of on-site interaction as $U = 70 \, \mathrm{meV}$, NN interaction as V = U/2, and NNN interaction as V' = U/4. We also consider different values of hole total filling factor $1.3 \lesssim \nu \lesssim 1.7$, and the displacement field in the range of $-80 \, \mathrm{meV} \le \varepsilon_D \le 0 \, \mathrm{meV}$. We proceed to solve the saddle-point equations in the U(1) slave spin approach, the details of which are explained in App. B.

A. Development of heavy Fermi liquid

The orbital resolved filling factors can be obtained from the U(1) slave spin approach, which are shown in Fig. 3(a). When the filling factor ν remains constant. there exists a range of displacement field strengths where the Mo layer orbitals are approximately pinned at unity filling ($\nu_{\text{Mo}} \sim 1$). Remarkably, the width of this interval does not vary significantly with the total filling factor, resulting in a "stripe" region highlighted by the red dashed lines in Fig. 3(a), which resembles the experimental observation [see Fig. 11 in App. F for reference]. To demonstrate this clearly, we also provide the orbital resolved filling factors as functions of the displacement field potential ε_D with fixed total filling factor $\nu = 1.4$ in Fig. 3(c). It is evident that the d orbital (Mo) filling exhibits a distinct "plateau" pattern when ε_D is varied, corresponding to the stripe region in Fig. 3(a). We also observed that the width of the stripe region in the phase diagram is around $\Delta \varepsilon_D \lesssim 30 \,\mathrm{meV}$, which is clearly smaller than the

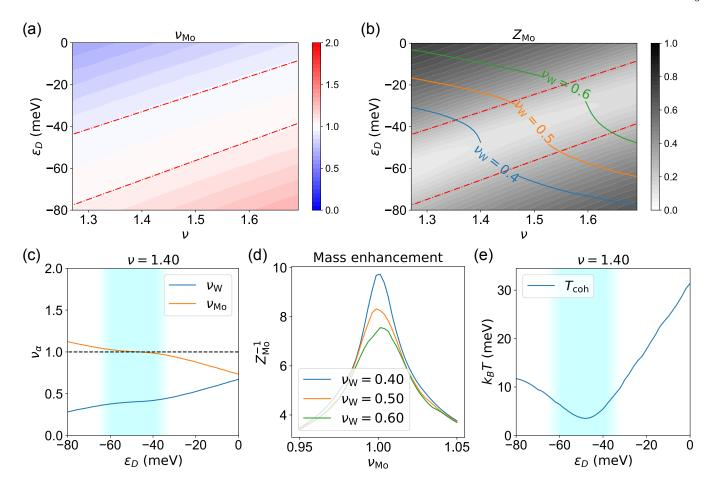


FIG. 3. (a) The orbital resolved filling factor of the heavy (Mo) orbital ν_{Mo} in the parameter space (ν, ε_D) . In the region labeled by the red dashed lines, the d orbital is almost at half filling $\nu_{\text{Mo}} \approx 1$. (b) The quasiparticle weight of the d orbital Z_{Mo} in the parameter space (ν, ε_D) . The conduction-band filling factors ν_{W} are constants along the three solid lines. (c) The filling factors of the two orbitals at a fixed total filling $\nu = 1.4$ with varying displacement field. The heavy Fermi liquid region is highlighted with light blue. (d) The mass enhancement (inverse of the quasiparticle weight Z^{-1}) of the d orbital as a function of d orbital filling, with multiple fixed conduction orbital fillings. (e) The coherence temperature scale evaluated with fixed total filling factor $\nu = 1.4$. We choose the strength of on-site interaction as U = 70 meV, NN interaction V = U/2, and NNN interaction V' = U/4.

on-site Hubbard interaction $U = 70 \,\mathrm{meV}$. This could be attributed to the large bandwidth of the d orbital.

Similar to the determination of orbital resolved filling factors, the evaluation of orbital resolved quasiparticle weight for the d orbital Mo is also accessible through the slave spin approach, the results of which are shown in Fig. 3(b). This quasiparticle weight Z_{Mo} drops significantly to $Z_{\mathrm{Mo}} \lesssim 0.2$ within the heavy Fermi liquid region. To demonstrate how the d orbitals are screened by the conduction electrons, we plot the mass enhancement of the heavy band, which is defined as the inverse of the quasiparticle weight, with different conduction electron densities in Fig. 3(d). The effective mass always approaches its maximum value at $\nu_{\text{Mo}} = 1$, and becomes smaller if the d orbital is doped away from half-filling. We also notice that the maximum value of the effective mass decreases with an increasing conduction electron density, because of the stronger screening. This picture

is captured by the schematic phase diagram in Fig. 1(b).

The large mass enhancement for the d orbital could potentially account for the experimentally observed narrow bandwidth of the Mo bands [3], whose corresponding effective mass $m_{\text{Mo}}^* \approx 5 \sim 10 m_e$ is an order of magnitude larger than the value $m_{\text{Mo}} \approx 0.65 m_e$ predicted by the non-interacting continuum model [16, 23]. In contrast, the quasiparticle weight of the conduction electron [see Fig. 8(a) in App. C] remains relatively high with $Z \gtrsim 0.8$ across the entire parameter space examined. Consequently, the effective mass $m_{\text{W}}^* \approx 0.5 m_e$ is similar to the value $m_{\text{W}} \approx 0.35 m_e$ predicted in the non-interacting theory.

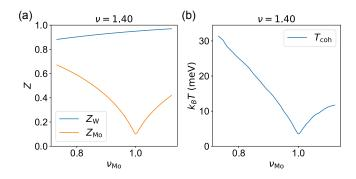


FIG. 4. (a) The quasiparticle weights of both orbitals as functions of the heavy fermion filling factor ν_{Mo} . (b) The coherence temperature scale as a function of the heavy fermion filling factor. The total filling factor in both figures is fixed to be $\nu=1.4$. The on-site interaction is chosen to be $U=75\,\text{meV}$ and $V=U/2,\,V'=U/4$.

B. Coherence temperature scale

The coherence temperature $T_{\rm coh}$, which characterizes the onset of Kondo screening as temperature is lowered, can be estimated from the effective bandwidth of the d orbital in the zero temperature slave fermion Hamiltonian [77–79]. In practice, this "bandwidth" can also be estimated from the inverse of the local density of states of the slave fermion, which will be explained in detail in App. C.

Normally, one would expect that the Kondo screening temperature scale is on the order of $\frac{1}{2}D_{\rm W}\exp(-\frac{D_{\rm W}}{J_{\rm K}})$ [45]. The Kondo coupling can be estimated by $J_K\sim t_{cd}^2/\Delta$ in which $t_{cd}\approx 1.5\,{\rm meV}$ is the hybridization, and Δ is the activation gap. Hence, the Kondo coupling strength is expected to be $J_K\lesssim 5\,{\rm meV}$, resulting in a very low screening temperature scale of $\lesssim 0.1\,{\rm K}$. Alternatively, in Kondo lattice systems, the coherence temperature of a metallic Kondo screened phase is controlled by $T_{\rm coh}\sim r^2/D_{\rm W}\sim 0.05\,{\rm K}$ [78], in which the renormalized hybridization is $r\sim \sqrt{Z_{\rm Mo}}t_{cd}\sim 5\,{\rm K}$. Both estimations lead to notably low temperature scales.

However, the coherence temperature has been extracted from resistivity measurements [3] to be much higher, $\approx 20 \sim 40\,\mathrm{K}$. Indeed, the bandwidth of the d orbital in hetero-bilayer TMDC is far from negligible, and thus the coherence temperature will depend on the quasiparticle weight Z_{Mo} in a different manner. As discussed in App. C, the coherence temperature can be estimated via the following expression when D_{Mo} is considered:

$$T_{\rm coh} \sim Z_{\rm Mo} D_{\rm Mo} + \frac{Z_{\rm Mo} Z_{\rm W} t_{cd}^2}{D_{\rm W}}$$
 (4)

Thus, much higher coherence temperatures become possible due to the dispersion of the heavy band. For fixed total filling factor $\nu=1.4$, the value of $T_{\rm coh}$ as a function of displacement field can be found in Fig. 3(e). In the heavy Fermi liquid region, the coherence temperature is

estimated to be at the order of magnitude of $T_{\rm coh} \sim 50 \, {\rm K}$. Notably, it aligns with the order of magnitude of $\sim 40 \, {\rm K}$ measured in the experiment. We also show that the quasiparticle weight of the d orbital and the coherence temperature (Fig. 4) approach their minimum when the d orbital is at half-filling.

IV. ORBITAL-SELECTIVE MOTT PHASE

An orbital-selective Mott phase (OSMP) develops when the d electrons are localized while the c electrons are itinerant. The transition from the heavy Fermi liguid into the OSMP can be achieved by tuning the total filling factor. In Figs. 5(a) and 5(b), we provide the d orbital filling factors and quasiparticle weights obtained with on-site interaction $U = 75 \,\mathrm{meV}$ at different total filling factors $\nu = 1.2, 1.4, 1.6$. The d orbital filling factors as functions of the displacement field, which are shown in Fig. 5(a), have "plateau" regions in certain ε_D intervals. The plateaus of different filling factors appear at different displacement field potential values, resulting in a stripe-shaped heavy Fermi liquid region, which is similar to what we obtained in Fig. 3(a). As one would expect from the lack of conduction electron screening, the heavy fermion quasiparticle weight can eventually be diminished to zero with a sufficiently low conduction electron density, which amplifies the contrast between the fate of (de)localization of the two orbitals. In Fig. 5(b) we present the displacement field dependent heavy fermion quasiparticle weight with different total filling factors. With smaller total electron densities, the minimum values of Z_{Mo} also get smaller, corresponding to the qualitative trend observed in Fig. 3(d). Indeed, Z_{Mo} drops to zero at its minimum point, indicating a transition into the OSMP with a destructed Kondo screening at $\nu = 1.2$.

We then discuss this transition into the OSMP along another axis with fixed displacement field potential $\varepsilon_D = -70 \,\mathrm{meV}$. In Fig. 5(c), we found that the d orbital filling factor is almost pinned at $\nu_{\mathrm{Mo}} = 1$ when the total filling is reduced to $\nu \leq 1.3$. It is also noticeable that the heavy fermion quasiparticle weight only drops to zero as the filling factor is further reduced to $\nu \leq 1.2$, as shown in Fig. 5(d).

We also note that the critical filling factor of the transition into the OSMP strongly depends on the strength of the interaction. For example, as we will discuss in App. E, total filling factor $\nu=1.4$ is in fact sufficiently low for an OSMP, if the on-site interaction is increased to $U=80\,\mathrm{meV}$.

As one would notice in Fig. 2(c), since the *d* orbitals effectively form a triangular lattice in the OSMP, the RKKY interaction might either be frustrated antiferromagnetic, or ferromagnetic at very low conduction electron density. The RKKY interaction could lead to either an anti-ferromagnetic ordered state [6, 7], a ferromagnetic ordered state [4], or a paramagnetic state in the local moment phase, depending on the competi-

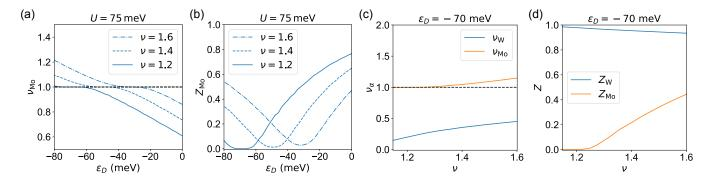


FIG. 5. (a) The orbital resolved filling factors of the Mo orbital as a function of displacement field with different total filling factors. Data shown by dash-dotted line, dashed line and solid lines are obtained with $\nu=1.6$, $\nu=1.4$ and $\nu=1.2$, respectively. (b) The quasiparticle weight of the Mo orbital as a function of displacement field. The total filling factors are the same as in (a). (c) The orbital resolved filling factors as functions of the total filling factor ν , with fixed displacement field potential $\varepsilon_D=-70\,\mathrm{meV}$. It can be seen that the d orbital Mo filling is almost pinned at $\nu_\mathrm{Mo}=1$ when $\nu\lesssim1.3$. (d) The quasiparticle weights as functions of the total filling factor ν with fixed displacement field. Orbital-selective Mott phase can be attained when $\nu\lesssim1.2$. The on-site, NN, and NNN interactions are chosen to be $U=75\,\mathrm{meV}$, V=U/2, and V'=U/4.

tion between the frustration strength and the screening strength as mentioned in Fig. 1(a). However, determining the magnetic order in the OSMP is beyond the scope of the present work.

V. DISCUSSION

We have analyzed the crossover into the heavy Fermi liquid state in the AB-stacked MoTe₂/WSe₂ bilayer moiré superlattices. In addition, we have described the transition from the heavy Fermi liquid state into the orbital-selective Mott phase that does not contain any long-range order.

To address the quantum critical physics, it is important to study the dynamical interplay between the Kondo

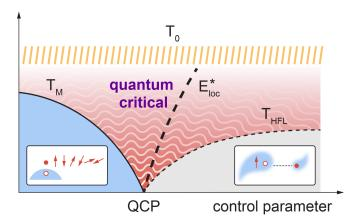


FIG. 6. Schematic finite temperature phase diagram near a quantum critical point (QCP) to be expected from a dynamical competition between Kondo and RKKY interactions, based on the EDMFT studies of the Kondo lattice [53, 68]. The cartoons for the heavy Fermi liquid and Kondo-destroyed phases are adapted from Ref. [60].

effect and RKKY interactions. To put the Kondo physics of the AB-stacked MoTe₂/WSe₂ in context, we recall that, in the correlation regime captured by the Kondo lattice model, studies based the extended dynamical mean field theory (EDMFT) showed that the RKKY interactions compete against the Kondo effect [53–55]. A new energy scale, E_{loc}^* , emerges, characterizing the destruction of the Kondo effect. As illustrated in Fig. 6, this scale separates two regimes of the phase diagram spanned by temperature and a non-thermal control parameter. To the right of the E_{loc}^* line, the system flows towards a heavy Fermi liquid ground state. The low-energy physics of the heavy quasiparticles and the associated large Fermi surface is characterized by the heavy Fermi liquid temperature scale, $T_{\rm HFL}$. The vanishing of the $T_{\rm HFL}$ scale at the QCP signifies the loss of quasiparticles. To the left of the E_{loc}^* line, the system flows towards a ground state in which the Kondo singlet is destroyed and the Fermi surface becomes small. Accordingly, the E_{loc}^* line characterizes the localization-delocalization of the heavy fermions. The role of long-range order depends on where the system lies in the global phase diagram. For example, along trajectory "I" of Fig. 1(a), the onset of the magnetic order is concurrent with the destruction of the Kondo effect. This is also illustrated in Fig. 6. Finally, the vestige of the coherence temperature is characterized by the temperature scale T_0 where the initial onset of the Kondo effect takes place as the temperature is lowered. These salient properties have been extensively evidenced by experiments in heavy fermion materials, including the dynamical scaling [56, 60, 80], Fermi surface crossover across a T^* temperature scale (associated with the E_{loc}^* energy scale) and its extrapolated zerotemperature jump [57, 58, 81], a linear-in-T relaxation rate that connects with the T-linear electrical resistivity [82–84] and related properties [59, 85] and, finally, the loss of quasiparticles [61].

The analysis presented here indicates that the AB-

stacked hetero-bilayer TMDC opens up a new correlation regime of Kondo destruction. Our findings raises the theoretical question about the dynamical competition between the Kondo/hybridization and RKKY interactions in this correlation regime, which is left for future work. Our results also motivate new opportunities for experimental studies, namely to explore the dynamical signatures of Kondo destruction outlined above in the AB-stacked hetero-bilayer TMDC and related moiré structures.

VI. SUMMARY

In this work, we studied an effective model that can well describe the Kondo physics in the AB-stacked MoTe₂/WSe₂ hetero-bilayer system. This effective model can be expressed as an extended Hubbard Hamiltonian with d and c orbitals, which correspond to moiré bands from the MoTe₂ and WSe₂ layers, respectively. The bandwidths of the two moiré bands differ by a factor of ~ 2 , which could lead to orbital-selective correlation effects. The hybridization between the two orbitals is also taken into consideration. The Hubbard Hamiltonian can describe the charge transfer between orbitals with strong displacement fields, which is not captured by the Kondo lattice Hamiltonian. Interaction in the c orbitals and the bandwidth associated with the d orbitals are also usually not addressed in previous studies. Hence, we believe that the two-orbital extended Hubbard Hamiltonian is the most suitable model for understanding the Kondodriven phenomena in this moiré structure without unnecessary complexity.

We then use a saddle-point approach to solve this effective interacting Hamiltonian. Using the total electron filling factor and the displacement field as tunable parameters, we identify the crossover into a heavy Fermi liquid in the phase diagram, which resembles the experimentally observed results [3]. With the d orbital bandwidth considered, our numerical study can also explain the heavy electron mass $m_{\rm Mo} \approx 10 m_e$ and the high coherence temperature $T_{\rm coh} \approx 20 \sim 40 \, {\rm K}$, which have been observed in transport measurements, providing a consistent interpretation. These results indicate that the Kondo effect in this system is in an extended correlation regime that goes beyond the canonical Kondo-lattice description.

We have also explored the consequence of doping the d orbital away from half filling. This doping, $\delta = \nu_d - 1$, serves as a new axis of the heavy fermion phase diagram. The numerical results have shown that the heavy Fermi liquid states with a very small $Z_{\rm Mo}$ can still exist in a narrow window when $\delta = \nu_d - 1 \neq 0$. When the d or-

bital is doped noticeably away from half filling, a small displacement field change can lead to a drastic change of its value, and the heavy fermion quasiparticle weight as well as the coherence temperature will be significantly increased. These phenomena have also been observed in the experiments as well.

In addition, our approach captures the orbital-selective Mott phase, in which the d electrons are localized while the c electrons remain itinerant. Our saddle-point analysis shows a vanishing heavy fermion quasiparticle weight at sufficiently low electron density. This is also qualitatively in agreement with the recent experimental observation [4].

Our results set the stage to address the amplified quantum fluctuations that the Kondo effect may produce in these moiré structures and the new correlation regimes that they open up for the Kondo-destruction quantum criticality. As such, the TMDC moiré structures provides a new setting to explore the salient properties associated with the amplified quantum fluctuations, such as the dynamical $\hbar\omega/k_{\rm B}T$ scaling, the linear-in-T relaxation rate, and loss of quasiparticles.

ACKNOWLEDGMENTS

We thank Jennifer Cano, Kin Fai Mak, Jie Shan, and Wenjin Zhao for helpful discussions. This work has primarily been supported by the U.S. DOE, BES, under Award No. DE-SC0018197 (model construction, F.X. and L.C.), by the Air Force Office of Scientific Research under Grant No. FA9550-21-1-0356 (conceptualization and model calculation, F.X., L.C. and Q.S.), and by the Robert A. Welch Foundation Grant No. C-1411 and the Vannevar Bush Faculty Fellowship No. ONR-VB N00014-23-1-2870 (Q.S.). The majority of the computational calculations have been performed on the Shared University Grid at Rice funded by NSF under Grant No. EIA-0216467, a partnership between Rice University, Sun Microsystems, and Sigma Solutions, Inc., the Big-Data Private-Cloud Research Cyberinfrastructure MRI-award funded by NSF under Grant No. CNS-1338099, and the Extreme Science and Engineering Discovery Environment (XSEDE) by NSF under Grant No. DMR170109. We acknowledge the hospitality of the Kavli Institute for Theoretical Physics, supported in part by the National Science Foundation under Grant No. NSF PHY1748958, during the program "A Quantum Universe in a Crystal: Symmetry and Topology across the Correlation Spectrum." Q.S. acknowledges the hospitality of the Aspen Center for Physics, which is supported by NSF grant No. PHY-2210452.

Y. Cao, V. Fatemi, A. Demir, S. Fang, S. L. Tomarken, J. Y. Luo, J. D. Sanchez-Yamagishi, K. Watanabe,

- in magic-angle graphene superlattices, Nature **556**, 80 (2018).
- [2] Y. Cao, V. Fatemi, S. Fang, K. Watanabe, T. Taniguchi, E. Kaxiras, and P. Jarillo-Herrero, Unconventional superconductivity in magic-angle graphene superlattices, Nature 556, 43 (2018).
- [3] W. Zhao, B. Shen, Z. Tao, Z. Han, K. Kang, K. Watanabe, T. Taniguchi, K. F. Mak, and J. Shan, Gate-tunable heavy fermions in a moiré kondo lattice, Nature 616, 61 (2023).
- [4] W. Zhao, B. Shen, Z. Tao, S. Kim, P. Knüppel, Z. Han, Y. Zhang, K. Watanabe, T. Taniguchi, D. Chowdhury, J. Shan, and K. F. Mak, Emergence of ferromagnetism at the onset of moiré Kondo breakdown, arXiv e-prints, arXiv:2310.06044 (2023), arXiv:2310.06044 [cond-mat.str-el].
- [5] A. Dalal and J. Ruhman, Orbitally selective Mott phase in electron-doped twisted transition metaldichalcogenides: A possible realization of the Kondo lattice model, Physical Review Research 3, 043173 (2021).
- [6] A. Kumar, N. C. Hu, A. H. MacDonald, and A. C. Potter, Gate-tunable heavy fermion quantum criticality in a moiré kondo lattice, Phys. Rev. B 106, L041116 (2022).
- [7] D. Guerci, J. Wang, J. Zang, J. Cano, J. H. Pixley, and A. Millis, Chiral kondo lattice in doped MoTe₂/WSe₂ bilayers, Science Advances 9, eade7701 (2023).
- [8] T. Li, S. Jiang, B. Shen, Y. Zhang, L. Li, Z. Tao, T. Devakul, K. Watanabe, T. Taniguchi, L. Fu, J. Shan, and K. F. Mak, Quantum anomalous hall effect from intertwined moiré bands, Nature 600, 641 (2021).
- [9] T. Li, S. Jiang, L. Li, Y. Zhang, K. Kang, J. Zhu, K. Watanabe, T. Taniguchi, D. Chowdhury, L. Fu, J. Shan, and K. F. Mak, Continuous Mott transition in semiconductor moiré superlattices, Nature 597, 350 (2021).
- [10] A. Ghiotto, E.-M. Shih, G. S. S. G. Pereira, D. A. Rhodes, B. Kim, J. Zang, A. J. Millis, K. Watanabe, T. Taniguchi, J. C. Hone, L. Wang, C. R. Dean, and A. N. Pasupathy, Quantum criticality in twisted transition metal dichalcogenides, Nature 597, 345 (2021).
- [11] Y. Zeng, Z. Xia, K. Kang, J. Zhu, P. Knüppel, C. Vaswani, K. Watanabe, T. Taniguchi, K. F. Mak, and J. Shan, Integer and fractional Chern insulators in twisted bilayer MoTe2, arXiv e-prints, arXiv:2305.00973 (2023), arXiv:2305.00973 [cond-mat.mes-hall].
- [12] H. Park, J. Cai, E. Anderson, Y. Zhang, J. Zhu, X. Liu, C. Wang, W. Holtzmann, C. Hu, Z. Liu, T. Taniguchi, K. Watanabe, J.-h. Chu, T. Cao, L. Fu, W. Yao, C.-Z. Chang, D. Cobden, D. Xiao, and X. Xu, Observation of Fractionally Quantized Anomalous Hall Effect, arXiv e-prints, arXiv:2308.02657 [cond-mat.mes-hall].
- [13] J. Cai, E. Anderson, C. Wang, X. Zhang, X. Liu, W. Holtzmann, Y. Zhang, F. Fan, T. Taniguchi, K. Watanabe, Y. Ran, T. Cao, L. Fu, D. Xiao, W. Yao, and X. Xu, Signatures of fractional quantum anomalous hall states in twisted mote2, Nature 622, 63 (2023).
- [14] F. Xu, Z. Sun, T. Jia, C. Liu, C. Xu, C. Li, Y. Gu, K. Watanabe, T. Taniguchi, B. Tong, J. Jia, Z. Shi, S. Jiang, Y. Zhang, X. Liu, and T. Li, Observation of integer and fractional quantum anomalous hall effects in twisted bilayer mote₂, Phys. Rev. X 13, 031037 (2023).
- [15] F. Wu, T. Lovorn, E. Tutuc, and A. H. MacDonald, Hubbard Model Physics in Transition Metal Dichalcogenide

- Moiré Bands, Physical Review Letters **121**, 026402 (2018).
- [16] Y. Zhang, T. Devakul, and L. Fu, Spin-textured chern bands in ab-stacked transition metal dichalcogenide bilayers, Proceedings of the National Academy of Sciences 118, e2112673118 (2021).
- [17] J. Zang, J. Wang, J. Cano, and A. J. Millis, Hartree-fock study of the moiré hubbard model for twisted bilayer transition metal dichalcogenides, Phys. Rev. B 104, 075150 (2021).
- [18] J. Zang, J. Wang, J. Cano, A. Georges, and A. J. Millis, Dynamical Mean-Field Theory of Moiré Bilayer Transition Metal Dichalcogenides: Phase Diagram, Resistivity, and Quantum Criticality, Physical Review X 12, 021064 (2022).
- [19] T. Devakul and L. Fu, Quantum anomalous hall effect from inverted charge transfer gap, Phys. Rev. X 12, 021031 (2022).
- [20] Z. Dong and Y.-H. Zhang, Excitonic chern insulator and kinetic ferromagnetism in a MoTe₂/WSe₂ moiré bilayer, Phys. Rev. B 107, L081101 (2023).
- [21] N. Morales-Durán, N. C. Hu, P. Potasz, and A. H. Mac-Donald, Nonlocal Interactions in Moiré Hubbard Systems, Physical Review Letters 128, 217202 (2022).
- [22] H. Pan, M. Xie, F. Wu, and S. Das Sarma, Topological phases in ab-stacked MoTe₂/WSe₂: Z₂ topological insulators, chern insulators, and topological charge density waves, Phys. Rev. Lett. 129, 056804 (2022).
- [23] L. Rademaker, Spin-orbit coupling in transition metal dichalcogenide heterobilayer flat bands, Phys. Rev. B 105, 195428 (2022).
- [24] Y. Yang, M. Morales, and S. Zhang, Metal-insulator transition in transition metal dichalcogenide heterobilayer: accurate treatment of interaction, arXiv e-prints, arXiv:2306.14954 (2023), arXiv:2306.14954 [cond-mat.str-el].
- [25] V. Crépel, D. Guerci, J. Cano, J. H. Pixley, and A. Millis, Topological superconductivity in doped magnetic moiré semiconductors, arXiv e-prints, arXiv:2304.01631 (2023), arXiv:2304.01631 [cond-mat.supr-con].
- [26] J. Dong, J. Wang, P. J. Ledwith, A. Vishwanath, and D. E. Parker, Composite fermi liquid at zero magnetic field in twisted MoTe₂, Phys. Rev. Lett. 131, 136502 (2023).
- [27] J. Yu, J. Herzog-Arbeitman, M. Wang, O. Vafek, B. A. Bernevig, and N. Regnault, Fractional Chern Insulators vs. Non-Magnetic States in Twisted Bilayer MoTe₂, arXiv e-prints, arXiv:2309.14429 (2023), arXiv:2309.14429 [cond-mat.mes-hall].
- [28] L. Ye, S. Fang, M. Kang, J. Kaufmann, Y. Lee, C. John, P. M. Neves, S. Y. F. Zhao, J. Denlinger, C. Jozwiak, A. Bostwick, E. Rotenberg, E. Kaxiras, D. C. Bell, O. Janson, R. Comin, and J. G. Checkelsky, Hopping frustration-induced flat band and strange metallicity in a kagome metal, Nature Physics 10.1038/s41567-023-02360-5 (2024).
- [29] J. Huang, L. Chen, Y. Huang, C. Setty, B. Gao, Y. Shi, Z. Liu, Y. Zhang, T. Yilmaz, E. Vescovo, M. Hashimoto, D. Lu, B. I. Yakobson, P. Dai, J.-H. Chu, Q. Si, and M. Yi, Non-fermi liquid behaviour in a correlated flatband pyrochlore lattice, Nature Physics 10.1038/s41567-023-02362-3 (2024).
- [30] S. Adhitia Ekahana, Y. Soh, A. Tamai, D. Gosálbez-Martínez, M. Yao, A. Hunter, W. Fan, Y. Wang, J. Li,

- A. Kleibert, C. A. F. Vaz, J. Ma, Y. Xiong, O. V. Yazyev, F. Baumberger, M. Shi, and G. Aeppli, Anomalous quasi-particles in the zone center electron pocket of the kagomé ferromagnet Fe3Sn2, arXiv e-prints, arXiv:2206.13750 (2022), arXiv:2206.13750 [cond-mat.str-el].
- [31] A. Ramires and J. L. Lado, Emulating heavy fermions in twisted trilayer graphene, Phys. Rev. Lett. 127, 026401 (2021).
- [32] Z.-D. Song and B. A. Bernevig, Magic-angle twisted bilayer graphene as a topological heavy fermion problem, Phys. Rev. Lett. 129, 047601 (2022).
- [33] G.-D. Zhou, Y.-J. Wang, N. Tong, and Z.-D. Song, Kondo Phase in Twisted Bilayer Graphene – A Unified Theory for Distinct Experiments, arXiv e-prints , arXiv:2301.04661 (2023), arXiv:2301.04661 [condmat.str-el].
- [34] H. Hu, G. Rai, L. Crippa, J. Herzog-Arbeitman, D. Călugăru, T. Wehling, G. Sangiovanni, R. Valenti, A. M. Tsvelik, and B. A. Bernevig, Symmetric Kondo Lattice States in Doped Strained Twisted Bilayer Graphene, arXiv e-prints, arXiv:2301.04673 (2023), arXiv:2301.04673 [cond-mat.str-el].
- [35] H. Hu, B. A. Bernevig, and A. M. Tsvelik, Kondo lattice model of magic-angle twisted-bilayer graphene: Hund's rule, local-moment fluctuations, and low-energy effective theory, Phys. Rev. Lett. 131, 026502 (2023).
- [36] D. Călugăru, M. Borovkov, L. L. H. Lau, P. Coleman, Z.-D. Song, and B. A. Bernevig, Twisted bilayer graphene as topological heavy fermion: II. Analytical approximations of the model parameters, Low Temperature Physics 49, 640 (2023), arXiv:2303.03429 [cond-mat.str-el].
- [37] C. Huang, X. Zhang, G. Pan, H. Li, K. Sun, X. Dai, and Z. Meng, Evolution from quantum anomalous Hall insulator to heavy-fermion semimetal in magic-angle twisted bilayer graphene, arXiv e-prints, arXiv:2304.14064 (2023), arXiv:2304.14064 [cond-mat.str-el].
- [38] J. Yu, M. Xie, B. A. Bernevig, and S. Das Sarma, Magicangle twisted symmetric trilayer graphene as a topological heavy-fermion problem, Phys. Rev. B 108, 035129 (2023).
- [39] Y.-Z. Chou and S. Das Sarma, Kondo lattice model in magic-angle twisted bilayer graphene, Phys. Rev. Lett. 131, 026501 (2023).
- [40] L. L. H. Lau and P. Coleman, Topological Mixed Valence Model for Twisted Bilayer Graphene, arXiv e-prints , arXiv:2303.02670 (2023), arXiv:2303.02670 [cond-mat.str-el].
- [41] Y. Li, B. M. Fregoso, and M. Dzero, Topological Mixed Valence Model in Magic-Angle Twisted Bilayer Graphene, arXiv e-prints, arXiv:2309.03416 (2023), arXiv:2309.03416 [cond-mat.supr-con].
- [42] H. Hu and Q. Si, Coupled topological flat and wide bands: Quasiparticle formation and destruction, Science Advances 9, eadg0028 (2023).
- [43] L. Chen, F. Xie, S. Sur, H. Hu, S. Paschen, J. Cano, and Q. Si, Emergent flat band and topological Kondo semimetal driven by orbital-selective correlations, arXiv e-prints , arXiv:2212.08017 (2022), arXiv:2212.08017 [cond-mat.str-el].
- [44] L. Chen, F. Xie, S. Sur, H. Hu, S. Paschen, J. Cano, and Q. Si, Metallic quantum criticality enabled by flat bands in a kagome lattice, arXiv e-prints, arXiv:2307.09431 (2023), arXiv:2307.09431 [cond-mat.str-el].
- [45] A. C. Hewson, The Kondo problem to heavy fermions, 2

- (Cambridge university press, 1997).
- [46] S. Wirth and F. Steglich, Exploring heavy fermions from macroscopic to microscopic length scales, Nat. Rev. Mater. 1, 16051 (2016).
- [47] S. Paschen and Q. Si, Quantum phases driven by strong correlations, Nature Reviews Physics 3, 9 (2021).
- [48] S. Kirchner, S. Paschen, Q. Chen, S. Wirth, D. Feng, J. D. Thompson, and Q. Si, Colloquium: Heavy-electron quantum criticality and single-particle spectroscopy, Rev. Mod. Phys. 92, 011002 (2020).
- [49] H. Hu, L. Chen, and Q. Si, Quantum Critical Metals: Dynamical Planckian Scaling and Loss of Quasiparticles, arXiv e-prints, arXiv:2210.14183 (2022), arXiv:2210.14183 [cond-mat.str-el].
- [50] H.-H. Lai, S. E. Grefe, S. Paschen, and Q. Si, Weyl-Kondo semimetal in heavy-fermion systems, Proc. Natl. Acad. Sci. U.S.A. 115, 93 (2018).
- [51] S. Dzsaber, L. Prochaska, A. Sidorenko, G. Eguchi, R. Svagera, M. Waas, A. Prokofiev, Q. Si, and S. Paschen, Kondo insulator to semimetal transformation tuned by spin-orbit coupling, Phys. Rev. Lett. 118, 246601 (2017).
- [52] L. Chen, C. Setty, H. Hu, M. G. Vergniory, S. E. Grefe, L. Fischer, X. Yan, G. Eguchi, A. Prokofiev, S. Paschen, J. Cano, and Q. Si, Topological semimetal driven by strong correlations and crystalline symmetry, Nat. Phys. 18, 134101346 (2022).
- [53] Q. Si, S. Rabello, K. Ingersent, and J. L. Smith, Locally critical quantum phase transitions in strongly correlated metals, Nature 413, 804 (2001).
- [54] P. Coleman, C. Pépin, Q. Si, and R. Ramazashvili, How do fermi liquids get heavy and die?, Journal of Physics: Condensed Matter 13, R723 (2001).
- [55] T. Senthil, M. Vojta, and S. Sachdev, Weak magnetism and non-fermi liquids near heavy-fermion critical points, Phys. Rev. B 69, 035111 (2004).
- [56] A. Schröder, G. Aeppli, R. Coldea, M. Adams, O. Stockert, H. Löhneysen, E. Bucher, R. Ramazashvili, and P. Coleman, Onset of antiferromagnetism in heavy-fermion metals, Nature 407, 351 (2000).
- [57] S. Paschen, T. Lühmann, S. Wirth, P. Gegenwart, O. Trovarelli, C. Geibel, F. Steglich, P. Coleman, and Q. Si, Hall-effect evolution across a heavy-fermion quantum critical point, Nature 432, 881 (2004).
- [58] H. Shishido, R. Settai, H. Harima, and Y. Ōnuki, A drastic change of the fermi surface at a critical pressure in CeRhIn₅: dhva study under pressure, Journal of the Physical Society of Japan 74, 1103 (2005).
- [59] T. Park, F. Ronning, H. Q. Yuan, M. B. Salamon, R. Movshovich, J. L. Sarrao, and J. D. Thompson, Hidden magnetism and quantum criticality in the heavy fermion superconductor cerhin5, Nature 440, 65 (2006).
- [60] L. Prochaska, X. Li, D. C. MacFarland, A. M. Andrews, M. Bonta, E. F. Bianco, S. Yazdi, W. Schrenk, H. Detz, A. Limbeck, Q. Si, E. Ringe, G. Strasser, J. Kono, and S. Paschen, Singular charge fluctuations at a magnetic quantum critical point, Science 367, 285 (2020).
- [61] L. Chen, D. T. Lowder, E. Bakali, A. M. Andrews, W. Schrenk, M. Waas, R. Svagera, G. Eguchi, L. Prochaska, Y. Wang, C. Setty, S. Sur, Q. Si, S. Paschen, and D. Natelson, Shot noise in a strange metal, Science 382, 907 (2023), https://www.science.org/doi/pdf/10.1126/science.abg6100.
- [62] Q. Si, Global magnetic phase diagram and local quantum criticality in heavy fermion metals, Physica B: Condensed

- Matter 378-380, 23 (2006), proceedings of the International Conference on Strongly Correlated Electron Systems.
- [63] Q. Si, Quantum criticality and global phase diagram of magnetic heavy fermions, physica status solidi (b) 247, 476 (2010).
- [64] P. Coleman and A. H. Nevidomskyy, Frustration and the kondo effect in heavy fermion materials, Journal of Low Temperature Physics 161, 182 (2010).
- [65] J. H. Pixley, R. Yu, and Q. Si, Quantum phases of the Shastry-Sutherland Kondo lattice: Implications for the global phase diagram of heavy-fermion metals, Phys. Rev. Lett. 113, 176402 (2014).
- [66] S. J. Yamamoto and Q. Si, Metallic ferromagnetism in the kondo lattice, Proceedings of the National Academy of Sciences 107, 15704 (2010).
- [67] Y. Komijani and P. Coleman, Model for a ferromagnetic quantum critical point in a 1d kondo lattice, Phys. Rev. Lett. 120, 157206 (2018).
- [68] Q. Si, J. H. Pixley, E. Nica, S. J. Yamamoto, P. Goswami, R. Yu, and S. Kirchner, Kondo destruction and quantum criticality in kondo lattice systems, Journal of the Physical Society of Japan 83, 061005 (2014).
- [69] R. Yu and Q. Si, U(1) slave-spin theory and its application to mott transition in a multiorbital model for iron pnictides, Phys. Rev. B **86**, 085104 (2012).
- [70] G.-B. Liu, W.-Y. Shan, Y. Yao, W. Yao, and D. Xiao, Three-band tight-binding model for monolayers of groupvib transition metal dichalcogenides, Phys. Rev. B 88, 085433 (2013).
- [71] A. Kormányos, G. Burkard, M. Gmitra, J. Fabian, V. Zólyomi, N. D. Drummond, and V. Fal'ko, k·p theory for two-dimensional transition metal dichalcogenide semiconductors, 2D Materials 2, 022001 (2015).
- [72] R. Bistritzer and A. H. MacDonald, Moiré bands in twisted double-layer graphene, Proceedings of the National Academy of Sciences 108, 12233 (2011).
- [73] B. Bradlyn, L. Elcoro, J. Cano, M. G. Vergniory, Z. Wang, C. Felser, M. I. Aroyo, and B. A. Bernevig, Topological quantum chemistry, Nature 547, 298 (2017).
- [74] S. R. Hassan and L. de' Medici, Slave spins away from half filling: Cluster mean-field theory of the hubbard and extended hubbard models, Phys. Rev. B 81, 035106 (2010).
- [75] Y.-M. Xie, C.-P. Zhang, and K. T. Law, Topological p_x+ip_y inter-valley coherent state in Moiré MoTe₂/WSe₂ heterobilayers, arXiv e-prints, arXiv:2206.11666 (2022), arXiv:2206.11666 [cond-mat.mtrl-sci].
- [76] T. Schork and S. Blawid, Periodic anderson model with correlated conduction electrons, Phys. Rev. B 56, 6559 (1997).
- [77] P. Nozières, Some comments on Kondo lattices and the

- Mott transition, The European Physical Journal B 6, 447 (1998).
- [78] S. Burdin, A. Georges, and D. R. Grempel, Coherence scale of the Kondo lattice, Physical Review Letters 85, 1048 (2000).
- [79] C. Kourris and M. Vojta, Kondo screening and coherence in kagome local-moment metals: Energy scales of heavy fermions in the presence of flat bands, arXiv e-prints, arXiv:2305.16198 (2023), arXiv:2305.16198 [cond-mat.str-el].
- [80] M. Aronson, R. Osborn, R. Robinson, J. Lynn, R. Chau, C. Seaman, and M. Maple, Non-Fermi-liquid scaling of the magnetic response in $UCu_{5-x}Pd_x$ (x = 1, 1.5), Phys. Rev. Lett. **75**, 725 (1995).
- [81] S. Friedemann, T. Westerkamp, M. Brando, N. Oeschler, S. Wirth, P. Gegenwart, C. Krellner, C. Geibel, and F. Steglich, Detaching the antiferromagnetic quantum critical point from the Fermi-surface reconstruction in YbRh₂Si₂, Nature Physics 5, 465 (2009).
- [82] D. H. Nguyen, A. Sidorenko, M. Taupin, G. Knebel, G. Lapertot, E. Schuberth, and S. Paschen, Superconductivity in an extreme strange metal, Nat. Commun. 12, 4341 (2021).
- [83] T. Park, V. A. Sidorov, F. Ronning, J.-X. Zhu, Y. Tokiwa, H. Lee, E. D. Bauer, R. Movshovich, J. L. Sarrao, and J. D. Thompson, Isotropic quantum scattering and unconventional superconductivity, Nature 456, 366 (2008).
- [84] P. Gegenwart, J. Custers, C. Geibel, K. Neumaier, T. Tayama, K. Tenya, O. Trovarelli, and F. Steglich, Magnetic-field induced quantum critical point in YbRh₂Si₂, Phys. Rev. Lett. 89, 056402 (2002).
- [85] G. Knebel, D. Aoki, J.-P. Brison, and J. Flouquet, The quantum critical point in CeRhIn₅: A resistivity study, Journal of the Physical Society of Japan 77, 114704 (2008).
- [86] G. Pizzi, V. Vitale, R. Arita, S. Blügel, F. Freimuth, G. Géranton, M. Gibertini, D. Gresch, C. Johnson, T. Koretsune, J. Ibañez-Azpiroz, H. Lee, J.-M. Lihm, D. Marchand, A. Marrazzo, Y. Mokrousov, J. I. Mustafa, Y. Nohara, Y. Nomura, L. Paulatto, S. Poncé, T. Ponweiser, J. Qiao, F. Thöle, S. S. Tsirkin, M. Wierzbowska, N. Marzari, D. Vanderbilt, I. Souza, A. A. Mostofi, and J. R. Yates, Wannier90 as a community code: new features and applications, Journal of Physics: Condensed Matter 32, 165902 (2020).
- [87] N. Marzari, A. A. Mostofi, J. R. Yates, I. Souza, and D. Vanderbilt, Maximally localized Wannier functions: Theory and applications, Reviews of Modern Physics 84, 1419 (2012).
- [88] R. Yu and Q. Si, Mott transition in multiorbital models for iron pnictides, Physical Review B 84, 235115 (2011).

CONTENTS

I. Introduction	1
A. AB-stacked MoTe ₂ /WSe ₂ hetero-bilayer B. Kondo effect	1
C. Kondo destruction	$\overset{2}{2}$
D. A new axis in the phase diagram	3

II. Model 3

		13
	A. Tight-binding model B. Interacting Hamiltonian	9
II.	Heavy Fermi liquid A. Development of heavy Fermi liquid B. Coherence temperature scale	5 7
V.	Orbital-selective Mott phase	7
V.	Discussion	8
VI.	Summary	9
	Acknowledgments	9
	References	S
A.	Model 1. Wannier functions of the non-interacting Hamiltonian 2. The projection of Coulomb interaction	13 13 14
В.	Method	16
C.	Coherence temperature	19
D.	Local density of states	20

Appendix A: Model

E. Orbital-selective Mott transition via strong interaction

F. Phase diagram in experiment

In this appendix, we provide a detailed discussion about the non-interacting Hamiltonian and its Wannier functions in App. A1. A brief review of the continuum model is discussed, and Wannier functions for the low-energy moiré bands can be constructed by analyzing their symmetry eigenvalues. The tight-binding model introduced in Sec. II A is based on the Wannier functions obtained from the continuum model.

The Coulomb interaction matrix elements discussed in App. A 2 are also based on the Wannier functions obtained from the continuum model. The effective interacting Hamiltonian in Eq. (3) is guided by these matrix elements as well.

1. Wannier functions of the non-interacting Hamiltonian

We first review the continuum model of twisted bilayer TMDC materials. In this system, the moiré superlattice is originated from the lattice mismatch between the MoTe₂ and WSe₂ layers. Both layers are hexagonal lattices with lattice constants $a_{\text{Mo}} \approx 3.575\text{Å}$ and $a_{\text{W}} \approx 3.32\text{Å}$ [16]. Therefore, the lattice constant of the moiré unit cell is $a_{\text{M}} = a_{\text{Mo}}a_{\text{W}}/(a_{\text{Mo}} - a_{\text{W}}) \approx 46.55\text{Å}$, which is much larger than the lattice constant of each individual layer. As a consequence, the reciprocal lattice of the moiré lattice is much smaller than the Brillouin zones of the single layers, which can be seen in Fig. 2(b). In this paper, we use $\mathbf{a}_1 = (0, a_M), \mathbf{a}_2 = (a_M/2, \sqrt{3}a_M/2)$ to represent the moiré lattice basis vectors, and use $\mathbf{b}_1 = (2\pi/a_M, -2\pi/\sqrt{3}a_M)$, $\mathbf{b}_2 = (0, 4\pi/\sqrt{3}a_M)$ to represent the corresponding reciprocal basis vectors.

Similar to the Bistritzer-MacDonald model for twisted bilayer graphene, we can also write down the Hamiltonian for AB-stacked bilayer $MoTe_2/WSe_2$ in a *single valley* as follows:

$$h = \begin{pmatrix} h_{\hat{d}}(-i\boldsymbol{\partial}) + V_{\hat{d}}(\mathbf{r}) - \frac{\varepsilon_D}{2} & W(\mathbf{r}) \\ W^*(\mathbf{r}) & h_{\hat{c}}(-i\boldsymbol{\partial}) + V_{\hat{c}}(\mathbf{r}) + \frac{\varepsilon_D}{2} \end{pmatrix}, \tag{A1}$$

21

21

	Γ_1	Γ_2	Γ_3	K_1	K_2	K_3	K'_1	K_2'	K_3'
\overline{E}	1	1	1	1	1	1	1	1	1
\overline{E} C_{3z}	1	ω	ω^*	1	ω	ω^*	1	ω^*	ω

TABLE I. The character table of irreps at high symmetry points of space group 143.

in which $h_{\hat{d}}$, $h_{\hat{c}}$ are the quadratic dispersion Hamiltonian of the individual layers:

$$h_{\hat{d},\hat{c}}(-i\boldsymbol{\partial}) = \frac{1}{2m_{\hat{d},\hat{c}}}\boldsymbol{\partial}^2. \tag{A2}$$

 $V_{\hat{d}}(\mathbf{r})$ and $V_{\hat{c}}(\mathbf{r})$ are the moiré potential received from the other layer, and $W(\mathbf{r})$ is the interlayer tunneling strength, which has the same period as the moiré superlattice. As mentioned in Ref. [16], the interlayer tunneling is strongly suppressed, since it is a spin-flipping process. Therefore, it is reasonable to build the Wannier functions for each layer individually.

Previous density functional theory studies have shown that the effective band mass of the MoTe₂ layer is $m_{\hat{d}} = 0.65m_e$, and the mass of the WSe₂ layer is $m_{\hat{c}} = 0.35m_e$, in which $m_e = 9 \times 10^{-31}$ kg is the bare electron mass [16]. The intralayer moiré potential has the following form:

$$V_{\hat{d},\hat{c}}(\mathbf{r}) = 2v_{\hat{d},\hat{c}} \sum_{i=1}^{3} \cos(\mathbf{g}_i \cdot \mathbf{r} + \phi_{\hat{d},\hat{c}}), \qquad (A3)$$

where $\mathbf{g}_i = C_3^{i-1}\mathbf{g}_1$ and $\mathbf{g}_1 = \mathbf{b}_1$ are the three smallest moiré reciprocal vectors along different directions. The eigenstates of the single layer Hamiltonian in the valley τ are Bloch states with the following form:

$$\psi_{\mathbf{k},\tau\alpha}(\mathbf{r}) = \frac{1}{\sqrt{\Omega_{\text{tot}}}} \sum_{\mathbf{Q}} u_{\mathbf{Q},\tau\alpha}(\mathbf{k}) e^{i(\mathbf{k}-\mathbf{Q})\cdot\mathbf{r}}.$$
 (A4)

Here **Q** stands for moiré lattice reciprocal vectors, and $\alpha = \hat{c}$, \hat{d} stands for the two types of fermions. The wavefunctions in the opposite valley $-\tau$ can be obtained via a time reversal transformation.

In the MoTe₂ layer, the values of these potential parameters are $v_{\hat{d}} = 4.1\,\mathrm{meV}$, $\phi_{\hat{d}} = 14^\circ$ [16]. Solving the kinetic Hamiltonian of this layer yields the band structure shown in Fig. 7(a). The C_{3z} eigenvalues of the three high symmetry points are also labeled. By comparing these eigenvalues with the little group irreps in Table I and the EBRs in Table II, we can find that this moiré band indeed corresponds to a local orbital on Wyckoff position 1a with site symmetry group representation 2E . Using Wannier90 [86] program with a trial wavefunction at this Wyckoff position and the angular momentum of 2E , we are able to find the proper gauge choice of the Bloch wavefunction $u_{\mathbf{Q},\tau\alpha}(\mathbf{k})$ which corresponds to the maximally localized Wannier function of the moiré band [87]. The real space distribution of its orbital has been shown in Fig. 7(b). Clearly that this orbital is highly concentrated within the size of a moiré unit cell.

It has been mentioned in Refs. [16, 22, 23] that the detail of the intralayer moiré potential of the WSe₂ layer $V_{\hat{c}}(\mathbf{r})$ is not crucial to the low energy physics. However, it still controls the little group representation at high symmetry points, since the gap opening around Γ and K is very sensitive to the phase $\phi_{\hat{c}}$. Fortunately, Ref. [16] provided the C_{3z} eigenvalues of the WSe₂ band at these high symmetry points, which indicates that $60^{\circ} \leq \phi_{\hat{c}} \leq 180^{\circ}$. Therefore, we use $v_{\hat{c}} \approx 5$ meV and $\phi_{\hat{c}} \approx 120^{\circ}$ as estimated values for the intralayer potential. The corresponding single layer band structure of WSe₂ layer can be found in Fig. 7(c). C_{3z} eigenvalues at high symmetry points also agree with the 2E elementary band representation at Wyckoff position 1c. We also show the Wannier orbital obtained by Wannier90 for the WSe₂ layer in Fig. 7(d). This explains why the two orbitals formed in two layers give rise to a hexagonal lattice, as depicted in Fig. 2(c) in the main text.

2. The projection of Coulomb interaction

In this subsection, we use some realistic parameters to estimate the interaction strength of our effective four-band model. With the Wannier wave functions obtained in the previous subsection, we are able to project the screened

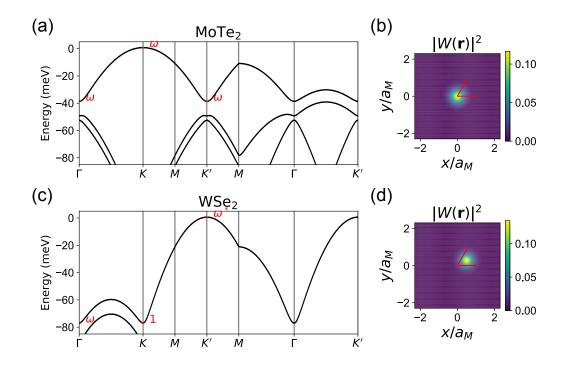


FIG. 7. (a) The single valley band structure of the MoTe₂ layer without interlayer tunneling considered. The band structure in the opposite valley can be obtained by simply applying time reversal transformation to the band structure in this valley. The (spinless) C_{3z} eigenvalues at high symmetry points Γ , K and K' are labeled, in which $\omega = e^{i\frac{2\pi}{3}}$. (b) The Wannier orbital of the highest band (the lowest hole band) in the MoTe₂ layer. (c) The single valley band structure of the WSe₂ layer without interlayer tunneling. (d) The Wannier orbital of the highest band in the WSe₂ layer. These wavefunctions are obtained via Wannier90 [86], and the red arrows represent the basis vectors of the Bravais moiré lattice \mathbf{a}_1 and \mathbf{a}_2 .

Wyckoff positions	1a			1b			1c		
EBR	$A_1 \uparrow G$	$^1E \uparrow G$	$^2E\uparrow G$	$A_1 \uparrow G$	$^1E \uparrow G$	$ ^2E\uparrow G$	$A_1 \uparrow G$	$1E \uparrow G$	$ ^2E\uparrow G$
Γ	Γ_1	Γ_3	Γ_2	Γ_1	Γ_3	Γ_2	Γ_1	Γ_3	Γ_2
\overline{K}	K_1	K_3	K_2	K_2	K_1	K_3	K_3	K_2	K_1
K'	K_1'	K_2'	K_3'	K_2'	K_3'	K_1'	K_3'	K_1'	K_2'

TABLE II. The elementary band representation of space group 143 of the three maximum Wyckoff positions.

Coulomb interaction into these low-energy orbitals. The projected interactions can be written as:

$$H_{I} = \frac{1}{2\Omega_{\text{tot}}} \sum_{\mathbf{k}\mathbf{k'}\mathbf{q} \in \text{MBZ}} \sum_{\tau\tau' = \pm} \sum_{\alpha\alpha' = \hat{c}, \hat{d}} U_{\alpha\alpha'}^{\tau\tau'}(\mathbf{q}; \mathbf{k}, \mathbf{k'}) \alpha_{\mathbf{k}+\mathbf{q}, \tau}^{\dagger} \alpha_{\mathbf{k}, \tau} \alpha_{\mathbf{k'}-\mathbf{q}, \tau'}^{\dagger} \alpha_{\mathbf{k'}, \tau'}^{\prime}. \tag{A5}$$

Here we still use $\tau, \tau' = \pm$ to represent the two valleys \mathcal{K} and \mathcal{K}' , and $\alpha, \alpha' = \hat{c}, \hat{d}$ to represent the two flavors (MoTe₂ layer and WSe₂ layer) of fermions. The interaction matrix elements $U_{\alpha\alpha'}^{\tau\tau'}(\mathbf{q}; \mathbf{k}, \mathbf{k}')$ can be written in the following form:

$$U_{\alpha\alpha'}^{\tau\tau'}(\mathbf{q}; \mathbf{k}, \mathbf{k}') = \sum_{\mathbf{G}} V(\mathbf{q} + \mathbf{G}) M_{\alpha}^{\tau}(\mathbf{k}, \mathbf{q} + \mathbf{G}) M_{\alpha'}^{\tau'}(\mathbf{k}', -\mathbf{q} - \mathbf{G}),$$
(A6)

in which **G** are reciprocal vectors of the moiré lattice. The Fourier transformed screened Coulomb potential has the form $V(\mathbf{q}) = (\xi e^2/4\varepsilon_0\varepsilon) \tanh(\xi q/2)/(\xi q/2)$, where we use $\xi \approx 10$ nm as the distance between the gates, and $\varepsilon \approx 10$ as the dielectric constant of the substrate. The form factors $M_{\alpha}^{\tau}(\mathbf{k}, \mathbf{q} + \mathbf{G})$ can be expressed by the inner products of

the non-interacting Bloch wave functions:

$$M_{\alpha}^{\tau}(\mathbf{k}, \mathbf{q} + \mathbf{G}) = \sum_{\mathbf{Q}} u_{\mathbf{Q} + \mathbf{G}, \tau\alpha}^{*}(\mathbf{k} + \mathbf{q}) u_{\mathbf{Q}, \tau\alpha}(\mathbf{k}), \qquad (A7)$$

where we have to use the gauge choice of $u_{\mathbf{Q},\tau\alpha}(\mathbf{k})$, which corresponds to the maximally localized Wannier states. Performing a discrete Fourier transformation into the Wannier function basis, this projected interacting Hamiltonian can also be written as:

$$H_{I} = \frac{1}{2} \sum_{\mathbf{R}_{0}} \sum_{\mathbf{R}\mathbf{D}\mathbf{D}'} \sum_{\tau\tau',\alpha\alpha'} \tilde{U}_{\alpha\alpha'}^{\tau\tau'}(\mathbf{R};\mathbf{D},\mathbf{D}') \alpha_{\mathbf{R}+\mathbf{D}+\mathbf{R}_{0},\eta,l}^{\dagger} \alpha_{\mathbf{R}+\mathbf{R}_{0},\eta,l} \alpha_{\mathbf{D}'+\mathbf{R}_{0},\eta',l'}^{\dagger} \alpha_{\mathbf{R}_{0},\eta',l'}^{\prime}.$$
(A8)

Obviously, the real space interaction elements are given by the following expression:

$$\tilde{U}_{\alpha\alpha'}^{\tau\tau'}(\mathbf{R}; \mathbf{D}, \mathbf{D}') = \frac{1}{\Omega_c N_M^3} \sum_{\mathbf{k}\mathbf{k}'\mathbf{q} \in MBZ} U_{\alpha\alpha'}^{\tau\tau'}(\mathbf{q}; \mathbf{k}, \mathbf{k}') e^{i\mathbf{q}\cdot(\mathbf{R}+\mathbf{D}-\mathbf{D}')} e^{i\mathbf{k}\cdot\mathbf{D}} e^{i\mathbf{k}'\cdot\mathbf{D}'}.$$
(A9)

Usually, two types of these projected interaction terms are considered when building an interacting lattice model. The first type of terms belongs to the direct channel with $\mathbf{D} = \mathbf{D}' = 0$:

$$\tilde{V}_{\alpha\alpha'}^{\tau\tau'}(\mathbf{R}) = \tilde{U}_{\alpha\alpha'}^{\tau\tau'}(\mathbf{R}; \mathbf{D} = 0, \mathbf{D}' = 0), \qquad (A10)$$

and the other type of terms belongs to the exchange channel with $\mathbf{D} = -\mathbf{D}' = -\mathbf{R} \neq 0$:

$$\tilde{J}_{\alpha}^{\tau\tau'}(\mathbf{R}) = -\tilde{U}_{\alpha\alpha}^{\tau\tau'}(\mathbf{R}; \mathbf{D} = -\mathbf{R}, \mathbf{D}' = \mathbf{R}). \tag{A11}$$

Using the Coulomb potential $V(\mathbf{q})$ and the Bloch state wave functions we obtained in the previous subsection, we numerically evaluated the values of some direct interaction terms, which can be found in Table III. The on-site interactions U of the two layers $\tilde{V}_{\hat{c}\hat{c}}(0)$ and $\tilde{V}_{\hat{d}\hat{d}}(0)$ are close but different. As a simplification, we use the same value for both layers in the actual calculation. The nearest-neighbor interaction $V = \tilde{V}_{\hat{c}\hat{d}}(0)$ approximately satisfies $V \approx U/2$, and the next-nearest-neighbor interaction $V' = \tilde{V}(\mathbf{a}_{1,2})$ is also around V/2. Hence, choosing $U = 70 \,\mathrm{meV}$, V = U/2 and V' = U/4 are reasonable estimations for these parameters. Since the screened Coulomb potential can change with the dielectric constant ε and the gate distance ξ , it is important to stress that these on-site, NN, and NNN interaction values should be regarded as reasonable estimations, and they can have different values in realistic materials.

On the other hand, the largest exchange term we obtained is only around $1.05\,\mathrm{meV}$, thus we ignored all the exchange interactions.

	$ \tilde{V}_{\hat{d}\hat{d}}(0) $	$\tilde{V}_{\hat{c}\hat{c}}(0)$	$ \tilde{V}_{\hat{c}\hat{d}}(0) $	$ ilde{V}_{\hat{d}\hat{d}}(\mathbf{a}_1)$	$ ilde{V}_{\hat{c}\hat{c}}(\mathbf{a}_1)$
Value (meV)	70.14	64.08	37.76	16.52	16.38

TABLE III. The numerical values of the largest direct interaction terms.

Appendix B: Method

To take into account the interaction effect, we utilize the U(1)-slave spin (SS) method [69] to solve the effective Hamiltonian described in Eqs. (1) and (3). We introduce the slave spin representation for a fermion operator as a product of an auxiliary bosonic operator o^{\dagger} and an auxiliary fermionic operator f^{\dagger} :

$$\alpha_{i\alpha\tau}^{\dagger} = o_{i\alpha\tau}^{\dagger} f_{i\alpha\tau}^{\dagger} \,. \tag{B1}$$

Here α^{\dagger} enumerates the creation operators of c orbitals c^{\dagger} or d orbitals d^{\dagger} . The auxiliary bosonic field $o^{\dagger}_{i\alpha\tau}=P^{+}_{i\alpha\tau}S^{+}_{i\alpha\tau}P^{-}_{i\alpha\tau}$ is represented by the product of a spin operator $S^{+}_{i\alpha\tau}$ and projection operators $P^{\pm}_{i\alpha\tau}=\frac{1}{\sqrt{1/2\pm S^{z}_{i\alpha\tau}}}$, which is suitable for a system away from half filling. By introducing these auxiliary operators, the physical Fock states can

be mapped to the enlarged Hilbert space of the slave fermion and slave spin operators:

$$|n_{i\alpha\tau} = 0\rangle \leftrightarrow |n_{i\alpha\tau}^f = 0\rangle |S_{i\alpha\tau}^z = \downarrow\rangle,$$

$$|n_{i\alpha\tau} = 1\rangle \leftrightarrow |n_{i\alpha\tau}^f = 1\rangle |S_{i\alpha\tau}^z = \uparrow\rangle,$$

$$\varnothing \leftrightarrow |n_{i\alpha\tau}^f = 0\rangle |S_{i\alpha\tau}^z = \uparrow\rangle,$$

$$\varnothing \leftrightarrow |n_{i\alpha\tau}^f = 1\rangle |S_{i\alpha\tau}^z = \downarrow\rangle.$$
(B2)

We notice that the introduction of the auxiliary operators expands the Hilbert space. Therefore, the following constraint is required to project out the unphysical states:

$$S_{i\alpha\tau}^z + \frac{1}{2} = n_{i\alpha\tau}^f. \tag{B3}$$

At the mean-field level, we treat this constraint on average by introducing the Lagrange multipliers $\lambda_{i\alpha\tau}$, such that $\langle S_{i\alpha\tau}^z \rangle + \frac{1}{2} = n_{i\alpha\tau}^f$. Note that in the physical Hilbert space, $n_{i\alpha\tau}^f = n_{i\alpha\tau}$. Using the slave fermion and spin operators, the kinetic Hamiltonian can be written as:

$$H_{0} = \sum_{\langle\langle i,j\rangle\rangle,\alpha\tau} t_{\alpha} e^{\tau i\phi_{ij}^{\alpha}} f_{i\alpha\tau}^{\dagger} o_{i\alpha\tau}^{\dagger} o_{j\alpha\tau} f_{j\alpha\tau} + \sum_{\langle i,j\rangle,\tau} \left(t_{cd} f_{ic\tau}^{\dagger} o_{ic\tau}^{\dagger} o_{jd\tau} f_{jd\tau} + \text{h.c.} \right) + \frac{\varepsilon_{D}}{2} \sum_{i\tau} \left(f_{ic\tau}^{\dagger} f_{ic\tau} - f_{id\tau}^{\dagger} f_{id\tau} \right). \tag{B4}$$

We can also decompose the product of auxiliary fermion and slave spin operators by the following equation:

$$f_{i\alpha\tau}^{\dagger} o_{i\alpha\tau}^{\dagger} o_{j\alpha'\tau'} f_{j\alpha'\tau'} = f_{i\alpha\tau}^{\dagger} f_{j\alpha'\tau'} \langle o_{i\alpha\tau}^{\dagger} o_{j\alpha'\tau'} \rangle + \langle f_{i\alpha\tau}^{\dagger} f_{j\alpha'\tau'} \rangle o_{i\alpha\tau}^{\dagger} o_{j\alpha'\tau'} + \text{h.c.}.$$
 (B5)

Furthermore, products of auxiliary bosonic operators can be decoupled via the single-site approximation $o^{\dagger}_{i\alpha\tau}o_{j\alpha'\tau'} = \langle o^{\dagger}_{i\alpha\tau}\rangle o_{j\alpha'\tau'} + o^{\dagger}_{i\alpha\tau}\langle o_{j\alpha'\tau'}\rangle - \langle o^{\dagger}_{i\alpha\tau}\rangle\langle o_{j\alpha'\tau'}\rangle$. By assuming that the bosonic operator expectation values are translation invariant $\langle o_{i\alpha\tau}\rangle = \langle o_{j\alpha\tau}\rangle = \langle o_{\alpha\tau}\rangle$, the two mean-field Hamiltonians for slave fermion and slave spin are given by:

$$H^{f} = \sum_{\langle\langle ij\rangle\rangle,\alpha\tau} t_{\alpha} e^{\tau i\phi_{ij}^{\alpha}} \langle o_{\alpha\tau}^{\dagger} \rangle \langle o_{\alpha\tau} \rangle f_{i\alpha\tau}^{\dagger} f_{i\alpha\tau} + \sum_{\langle i,j\rangle,\tau} \left(t_{cd} \langle o_{c\tau}^{\dagger} \rangle \langle o_{d\tau} \rangle f_{ic\tau}^{\dagger} f_{jd\tau} + \text{h.c.} \right) + \frac{\varepsilon_{D}}{2} \sum_{i\tau} \left(f_{ic\tau}^{\dagger} f_{ic\tau} - f_{id\tau}^{\dagger} f_{id\tau} \right),$$

$$H^{S} = \sum_{i\alpha\tau} \sum_{\mathbf{k}} \left(\epsilon_{\alpha}^{\tau} (\mathbf{k}) \langle f_{\mathbf{k}\alpha\tau}^{\dagger} f_{\mathbf{k}\alpha\tau} \rangle \langle o_{\alpha\tau} \rangle o_{i\alpha\tau}^{\dagger} + \text{h.c.} \right) + \sum_{i\tau} \sum_{\mathbf{k}} \left(\epsilon_{cd} (\mathbf{k}) \langle f_{\mathbf{k}c\tau}^{\dagger} f_{\mathbf{k}d\tau} \rangle \left(\langle o_{c\tau}^{\dagger} \rangle o_{id\tau} + o_{ic\tau}^{\dagger} \langle o_{d\tau} \rangle \right) + \text{h.c.} \right) + H_{I}^{S},$$

$$(B6)$$

where $\epsilon_{\alpha}^{\tau}(\mathbf{k})$ and $\epsilon_{cd}(\mathbf{k})$ are the Fourier transformation of the intra and inter-orbital hopping terms in the momentum space, respectively. We further perform the Taylor expansion of the projection operators $P_{i\alpha\tau}^{\pm}$ and bosonic operators $o_{i\alpha\tau}^{\dagger}$ by considering $\delta S_{i\alpha\tau}^z = S_{i\alpha\tau}^z - \langle S_{\alpha\tau}^z \rangle$ as a small parameter:

$$P_{i\alpha\tau}^{\pm} \approx \frac{1}{\sqrt{\frac{1}{2} \pm \langle S_{\alpha\tau}^{z} \rangle}} \left(1 \mp \frac{\delta S_{i\alpha\tau}^{z}}{\sqrt{\frac{1}{2} \pm \langle S_{\alpha\tau}^{z} \rangle}} \right) ,$$

$$o_{i\alpha\tau}^{\dagger} \approx \langle P_{\alpha\tau}^{+} \rangle S_{i\alpha\tau}^{+} \langle P_{\alpha\tau}^{-} \rangle + \langle P_{\alpha\tau}^{+} \rangle \langle S_{i\alpha\tau}^{+} \rangle \langle P_{\alpha\tau}^{-} \rangle \frac{1}{2} (S_{i\alpha\tau}^{z} - \langle S_{\alpha\tau}^{z} \rangle) \left(\frac{-1}{n_{\alpha\tau}} + \frac{1}{1 - n_{\alpha\tau}} \right) ,$$

$$= O_{i\alpha\tau}^{\dagger} + \langle O_{\alpha\tau}^{\dagger} \rangle \eta_{\alpha\tau} \left[2S_{i\alpha\tau}^{z} - (2n_{\alpha\tau} - 1) \right] ,$$
(B7)

where $O_{i\alpha\tau}^{\dagger} = \langle P_{\alpha\tau}^{+} \rangle S_{i\alpha\tau}^{+} \langle P_{\alpha\tau}^{-} \rangle$, $\eta_{\alpha\tau} = \frac{1}{2} \frac{n_{\alpha\tau} - 1/2}{(1 - n_{\alpha\tau})n_{\alpha\tau}}$, and $\langle o_{\alpha\tau} \rangle = \langle O_{\alpha\tau} \rangle$. Using these expansions, the slave spin Hamiltonian can be written as the following form:

$$H^{S} = \sum_{i\alpha\tau} \left(\tilde{\epsilon}_{\alpha} \langle O_{\alpha\tau} \rangle \left(O_{i\alpha\tau}^{\dagger} + \langle O_{\alpha\tau}^{\dagger} \rangle \eta_{\alpha\tau} [2S_{i\alpha\tau}^{z} - (2n_{\alpha\tau} - 1)] \right) + \text{h.c.} \right)$$

$$+ \sum_{i\tau} \left[\tilde{\epsilon}_{cd} \langle O_{c\tau}^{\dagger} \rangle \left(O_{id\tau} + \langle O_{d\tau} \rangle \eta_{d\tau} [2S_{id\tau}^{z} - (2n_{d\tau} - 1)] \right)$$

$$+ \tilde{\epsilon}_{cd} \left(O_{ic\tau}^{\dagger} + \langle O_{c\tau}^{\dagger} \rangle \eta_{c\tau} [2S_{ic\tau}^{z} - (2n_{c\tau} - 1)] \right) \langle O_{d\tau} \rangle + \text{h.c.} \right] + H_{I}^{S},$$
(B8)

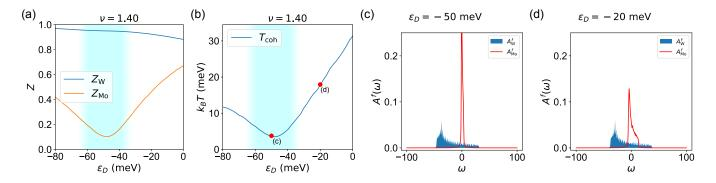


FIG. 8. (a) The quasiparticle weights of both the c and d orbitals as functions of the displacement field with fixed total hole filling factor $\nu=1.4$. (b) The coherent temperature scale $T_{\rm coh}$ estimated by slave fermion local density of states with fixed total hole filling factor $\nu=1.4$. Note that this figure is the same as Fig. 3(e) in the main text. (c) The slave fermion local density of states for both orbitals with displacement field $\varepsilon_D=-50\,{\rm meV}$, at which the d orbital filling factor is very close to $\nu_{\rm Mo}\approx 1$. (d) The slave fermion local density of states with displacement field $\varepsilon_D=-20\,{\rm meV}$, at which the d orbital filling factor $\nu_{\rm Mo}$ is away from half-filling. In these calculations we choose the on-site interaction strength $U=70\,{\rm meV}$.

in which $\tilde{\epsilon}_{\alpha} = \sum_{\mathbf{k}} \epsilon_{\alpha}(\mathbf{k}) \langle f_{\mathbf{k}\alpha\tau}^{\dagger} f_{\mathbf{k}\alpha\tau} \rangle$ and $\tilde{\epsilon}_{cd} = \sum_{\mathbf{k}} \epsilon_{cd}(\mathbf{k}) \langle f_{\mathbf{k}c\tau}^{\dagger} f_{\mathbf{k}d\tau} \rangle$. We use the relationship $2S_{i\alpha\tau}^z = f_{i\alpha\tau}^{\dagger} f_{i\alpha\tau} - 1$ to replace terms proportional to $S_{i\alpha\tau}^z$ and move them from H^S to H^f and combine the constraint Eq. (B3). This procedure could completely decouple the slave fermion and slave spin Hamiltonians:

$$H^{f} = \sum_{\langle\langle i,j\rangle\rangle,\tau} \left(\langle O_{c\tau}^{\dagger} \rangle \langle O_{c\tau} \rangle t_{c} e^{i\tau\phi_{ij}^{c}} f_{ic\sigma}^{\dagger} f_{jc\tau} + \text{h.c.} \right) + \sum_{\langle\langle i,j\rangle\rangle,\tau} \left(\langle O_{d\tau}^{\dagger} \rangle \langle O_{d\tau} \rangle t_{d} e^{i\tau\phi_{ij}^{d}} f_{id\sigma}^{\dagger} f_{jd\tau} + \text{h.c.} \right)$$

$$+ \sum_{\langle i,j\rangle\tau} \left(\langle O_{c\tau}^{\dagger} \rangle \langle O_{d\tau} \rangle t_{cd} f_{ic\tau}^{\dagger} f_{jd\tau} + \text{h.c.} \right)$$

$$+ \sum_{i\tau} \left(\frac{\epsilon_{D}}{2} - \mu - \lambda_{c\tau} + \lambda_{c\tau}^{0} \right) f_{ic\tau}^{\dagger} f_{ic\tau} + \left(\frac{-\epsilon_{D}}{2} - \mu - \lambda_{d\tau} + \lambda_{d\tau}^{0} \right) f_{id\tau}^{\dagger} f_{id\tau},$$

$$(B9)$$

$$H^{S} = \sum_{i\tau} \left[\tilde{\epsilon}_{c} \left(\langle O_{c\tau} \rangle O_{ic\tau}^{\dagger} + \text{h.c.} \right) + \tilde{\epsilon}_{d} \left(\langle O_{d\tau} \rangle O_{id\tau}^{\dagger} + \text{h.c.} \right) + \tilde{\epsilon}_{cd} \left(\langle O_{c\tau} \rangle O_{id\tau}^{\dagger} + \text{h.c.} \right) \right]$$

$$+ \sum_{i\tau\sigma} \lambda_{\alpha\tau} \left(S_{i\alpha\tau}^{z} + \frac{1}{2} \right) + H_{I}^{S}$$

where we further introduce the chemical potential μ to control the filling factor and $\lambda_{\alpha\tau}^0 = 2(\bar{\epsilon}_{\alpha\alpha} + \bar{\epsilon}_{\alpha\bar{\alpha}})\eta_{\alpha\tau}$, with $\bar{\epsilon}_{\alpha\alpha'} = \left(\tilde{\epsilon}_{\alpha\alpha'}\langle O_{\alpha\tau}\rangle\langle O_{\alpha'\tau}^{\dagger}\rangle + \text{c.c.}\right)$. The interaction part of the slave spin Hamiltonian H_I^S contains the on-site terms U, as well as the NN and NNN terms treated on the mean-field level:

$$H_I^S = \sum_{i} \left(\frac{U}{2} \sum_{\alpha} \left(\sum_{\tau} S_{i\alpha\tau}^z \right)^2 + V \sum_{\tau\tau'} \left(3S_{ic\tau}^z \langle S_{d\tau'}^z \rangle + 3\langle S_{c\tau}^z \rangle S_{id\tau'}^z \right) + V' \sum_{\alpha\tau\tau'} 6S_{i\alpha\tau}^z \langle S_{\alpha\tau'}^z \rangle \right) . \tag{B10}$$

The numbers 3 and 6 come from the coordination numbers of NN and NNN interactions. Due to the mean field treatment of these interaction terms, different unit cells in the slave spin Hamiltonian H^S become completely decoupled from each other:

$$H^S = \sum_i H_i^S \,. \tag{B11}$$

Thus the mean field equations can be solved self-consistently with effectively only one unit cell in the slave spin Hamiltonian, by assuming $\langle O_{\alpha\tau} \rangle$, $\lambda_{\alpha\tau}$ and μ as variational parameters. The quasiparticle weight associated with orbital α is described by $Z_{\alpha\tau} = \langle O_{\alpha\tau} \rangle \langle O_{\alpha\tau}^{\dagger} \rangle = |z_{\alpha\tau}|^2$ if the self-consistently solved value of $z_{\alpha\tau}$ is non-zero. If the expectation value $z_{\alpha\tau}$ drops to zero, the corresponding orbital $\alpha\tau$ loses the quasiparticle weight and becomes Mott insulating, and its orbital-resolved filling factor is also enforced to be half-filled. In the numerical calculation in the main text, we also assumed the expectation value $z_{\alpha\tau}$ is irrelevant to the valley (spin) index.

Appendix C: Coherence temperature

We consider the coherence temperature scale $T_{\rm coh}$ in the heavy Fermi liquid state. This temperature characterizes the finite temperature onset of the initial Kondo screening. It can be estimated in terms of the effective bandwidth of the d orbitals in the saddle-point calculation at zero temperature. Hence, a practical way [79] of estimating $T_{\rm coh}$ is using the inverse of the local density of states of the slave fermion: $k_B T_{\rm coh} = 1/A_{\rm Mo}^f(\omega = 0)$, in which $A_{\rm Mo}^f(\omega)$ corresponds to the "spectral function" of the d orbital slave fermion. Note that it is different from the local density of states of the physical fermions d^{\dagger} , which will be discussed in App. D. Since the slave fermion Hamiltonian H^f is a quadratic fermionic Hamiltonian, the local density of states of slave fermions can be easily obtained via the inverse of its "Bloch Hamiltonian":

$$A_{\alpha\tau}^{f}(\omega) = -\frac{1}{\pi} \operatorname{Im} \frac{1}{N} \sum_{\mathbf{k}} \left(\frac{1}{\omega + i0^{+} - h^{f}(\mathbf{k})} \right)_{\alpha\tau,\alpha\tau} , \tag{C1}$$

$$h^f(\mathbf{k}) = \begin{pmatrix} h_+^f(\mathbf{k}) \\ h_-^f(\mathbf{k}) \end{pmatrix}, \tag{C2}$$

$$h_{\tau}^{f}(\mathbf{k}) = \begin{pmatrix} Z_{\text{Mo}} \epsilon_{d}^{\tau}(\mathbf{k}) - \lambda_{d} + \lambda_{d}^{0} - \frac{\varepsilon_{D}}{2} - \mu & \sqrt{Z_{\text{Mo}}} Z_{\text{W}} \epsilon_{cd}(\mathbf{k}) \\ \sqrt{Z_{\text{Mo}}} Z_{\text{W}} \epsilon_{cd}^{*}(\mathbf{k}) & Z_{\text{W}} \epsilon_{c}^{\tau}(\mathbf{k}) - \lambda_{c} + \lambda_{c}^{0} + \frac{\varepsilon_{D}}{2} - \mu \end{pmatrix},$$
(C3)

in which $\epsilon_d^{\tau}(\mathbf{k})$, $\epsilon_c^{\tau}(\mathbf{k})$, and $\epsilon_{cd}(\mathbf{k})$ are the Fourier transformation of the real space hoppings $t_d e^{i\tau\phi_{ij}^d}$, $t_c e^{i\tau\phi_{ij}^c}$ and t_{cd} , respectively.

In particular, if we assume the d orbitals are exactly flat with vanishing bandwidth $[\epsilon_d(\mathbf{k}) \to 0]$ and the c orbitals are non-interacting $(Z_W = 1)$, the slave fermion Hamiltonian can be approximately written in the following form:

$$h_{\tau}^{f}(\mathbf{k}) \sim \begin{pmatrix} 0 & \sqrt{Z_{\text{Mo}}} \epsilon_{cd}(\mathbf{k}) \\ \sqrt{Z_{\text{Mo}}} \epsilon_{cd}^{*}(\mathbf{k}) & \epsilon_{c}^{\tau}(\mathbf{k}) + \mathcal{E}_{c} \end{pmatrix}$$
 (C4)

Here \mathcal{E}_c contains the contributions from Lagrange multipliers λ_c , λ_c^0 , chemical potential μ and displacement field ε_D , such that the dispersion of $\epsilon_c^{\tau}(\mathbf{k}) + \mathcal{E}_c$ crosses the Fermi level with the correct filling factor. We assume the off-diagonal elements are perturbative, and the two eigenvalues of the matrix $h_{\tau}^f(\mathbf{k})$ are:

$$\omega_{+}(\mathbf{k}) \sim \epsilon_{c}(\mathbf{k}) + \mathcal{E}_{c}$$
, (C5)

$$\omega_{-}(\mathbf{k}) \sim -\frac{Z_{\text{Mo}}|\epsilon_{cd}(\mathbf{k})|^2}{\epsilon_{c}(\mathbf{k}) + \mathcal{E}_c},$$
 (C6)

in which the dominant component of the eigenvector for $\omega_{-}(\mathbf{k})$ corresponds to the d orbital. Thus, charge excitations that exhibit a significant overlap with the d orbital are predominantly distributed within an energy interval with a width denoted as $k_B T_{\rm coh} \sim \frac{Z_{\rm Mo} t_{cd}^2}{D_{\rm W}}$, where $D_{\rm W}$ is the bandwidth of the conduction band. This expression resembles the definition of the coherence temperature scale $T^* \sim r^2/D_c$ introduced in Ref. [78].

However, the realistic Hamiltonian of the hetero-bilayer TMDC does not have a vanishing d orbital dispersion. In contrast, the bandwidth of the d orbital D_{Mo} is much larger than the hybridization t_{cd} . If the bandwidth of the heavy band is taken into account, the coherent temperature scale has to be estimated from the following matrix:

$$h_{\tau}^{f}(\mathbf{k}) \sim \begin{pmatrix} Z_{\text{Mo}} \epsilon_{d}^{\tau}(\mathbf{k}) + \mathcal{E}_{d} & \sqrt{Z_{\text{W}}} Z_{\text{Mo}} \epsilon_{cd}(\mathbf{k}) \\ \sqrt{Z_{\text{W}}} Z_{\text{Mo}} \epsilon_{cd}^{*}(\mathbf{k}) & Z_{\text{W}} \epsilon_{c}^{\tau}(\mathbf{k}) + \mathcal{E}_{c} \end{pmatrix} . \tag{C7}$$

If the hybridization terms in the off-diagonal elements are still treated as perturbations, the eigenvalue that is dominated by the d orbital will be:

$$\omega_{-}(\mathbf{k}) \sim Z_{\text{Mo}}[\epsilon_d(\mathbf{k}) + \mathcal{E}_d] - \frac{Z_{\text{Mo}}Z_{\text{W}}|\epsilon_{cd}(\mathbf{k})|^2}{\epsilon_c(\mathbf{k}) + \mathcal{E}_c}.$$

Consequently, the coherent temperature scale is different from the case with exact flat heavy bands, and it can be estimated as follows:

$$k_B T_{\rm coh} \sim Z_{\rm Mo} D_{\rm Mo} + \frac{Z_{\rm Mo} Z_{\rm W} t_{cd}^2}{D_{\rm W}}.$$
 (C8)

When compared with the exact flat band case $t_d = 0$, it is significantly increased by the bandwidth of the d orbital.

By calculating the local density of states of the slave fermions, we are able to get the coherence temperature with different displacement field strength values. The results can be found in Fig. 8(b). Observing the plot, it becomes evident that $T_{\rm coh}$ closely resembles the curve of the quasiparticle weight multiplied by a factor that is approximately equal to the d orbital bandwidth, and $T_{\rm coh}$ in the heavy Fermi liquid region is strongly suppressed to $k_B T_{\rm coh} \sim 5 \, {\rm meV}$. In contrast, when the d orbital filling factor is doped far away from $\nu_{\rm Mo} = 1$, the heavy fermion quasiparticle weight gets large and thus the coherent temperature can approach $T_{\rm coh} \gtrsim 100 \, {\rm K}$.

As a reference, we also show the slave fermion local density of states for both orbitals at two points in the phase diagram in Figs. 8(c-d). The local density of states in Fig. 8(c) is obtained with $\varepsilon_D = -50\,\mathrm{meV}$ and $\nu = 1.4$, which is in the heavy Fermi liquid region, while in Fig. 8(d), the local density of states is obtained outside of the heavy Fermi liquid region. The heavy Fermi liquid state has a narrower heavy band and a higher slave fermion density of states at $\omega = 0$, and thus a much lower T_{coh} .

Appendix D: Local density of states

The local density of states shown in the previous appendix is obtained from the slave fermion operators $f_{\hat{c}}^{\dagger}$ or $f_{\hat{d}}^{\dagger}$, instead of the physical fermions c^{\dagger} or d^{\dagger} . Local charge fluctuation is not considered, and hence the lower and upper Hubbard bands are not captured. To correctly describe the local charge fluctuation, slave spin excited states need to be considered.

We write the physical fermion operators as the product of slave fermion operator and slave spin operator, and we write the many-body eigenstates as tensor products of the local slave spin eigenstates and Slater determinants of slave fermion states. Hence, the local density of states of the physical degrees of freedom can be obtained from the following expression, which has been derived in Ref. [88]:

$$A_{\alpha\tau}(\omega) = \frac{1}{N} \sum_{\mathbf{k}} \sum_{m} \left(\sum_{i, \epsilon_{\mathbf{k}, i} > 0} \delta(\omega + E_g - E_m - \epsilon_{\mathbf{k}, i}) |u_{\alpha\tau, i}(\mathbf{k})|^2 \frac{|\langle m|S_{\alpha\tau}^+|g\rangle|^2}{n_{\alpha\tau} (1 - n_{\alpha\tau})} \mathcal{F}_{\alpha\tau, m}^+ \right)$$

$$+ \sum_{i, \epsilon_{\mathbf{k}, i} < 0} \delta(\omega - E_g + E_m - \epsilon_{\mathbf{k}, i}) |u_{\alpha\tau, i}(\mathbf{k})|^2 \frac{|\langle m|S_{\alpha\tau}^-|g\rangle|^2}{n_{\alpha} (1 - n_{\alpha\tau})} \mathcal{F}_{\alpha\tau, m}^- \right),$$
(D1)

$$\mathcal{F}_{\alpha\tau,m}^{+} = \begin{cases} 1 & m = g \\ \frac{1 - Z_{\alpha\tau}}{n_{\alpha\tau}^{-1} - Z_{\alpha\tau}} & m \neq g \end{cases} , \tag{D2}$$

$$\mathcal{F}_{\alpha\tau,m}^{-} = \begin{cases} 1 & m = g \\ \frac{1 - Z_{\alpha\tau}}{(1 - n_{\alpha\tau})^{-1} - Z_{\alpha\tau}} & m \neq g \end{cases}$$
 (D3)

Here we use E_m and $|m\rangle$ to represent the eigenvalues and eigenstates of the local slave spin Hamiltonian H_i^S , and the summation over $|m\rangle$ includes all the eigenstates of H_i^S . Specifically, the ground state of H_i^S is denoted by $|g\rangle$. We also use $\epsilon_{\mathbf{k},i}$, $u_{\alpha\tau,i}(\mathbf{k})$ to represent the *i*-th eigenvalue and eigenvector of the slave fermion Hamiltonian $h^f(\mathbf{k})$. The factors $\mathcal{F}_{\alpha\tau}^{\pm}$ guarantee that Eq. (D1) satisfy the following sum rules of the spectral functions:

$$\int_{-\infty}^{\infty} d\omega A_{\alpha\tau}(\omega) = 1, \qquad (D4)$$

$$\int_{-\infty}^{0} d\omega A_{\alpha\tau}(\omega) = n_{\alpha\tau} \,. \tag{D5}$$

Using the self-consistent solutions of the slave spin and slave fermion Hamiltonians, we numerically evaluated the local density of states for both the c and d orbitals with the same parameters as in Figs. 8(c-d). The results can be found in Fig. 9. In both the heavy Fermi liquid state (a) and normal Fermi liquid state (b), the spectral peaks of the d orbital near $\omega=0$ are lower than the peak in the slave fermion local density of states, which is a consequence of a small $Z_{\rm Mo}$. The incoherent upper and lower Hubbard bands separated by U are clearly visible in both cases. Since the bare bandwidth of the d orbital is not negligible when compared with U, the coherent peak of $A_{\rm Mo}(\omega)$ near the Fermi energy starts getting wider noticeably when the upper Hubbard band moves close to $\omega=0$, even if it is still obviously above $\omega=0$, as seen in Fig. 9(b). This indicates a large quasiparticle weight and a reduced effective mass for the heavy fermion. As a result, the width of the heavy Fermi liquid region along the displacement field potential axis $\Delta \varepsilon_D$, in which the quasiparticle weight of the Mo orbital remains very small ($Z_{\rm Mo} \ll 1$), will be narrower than

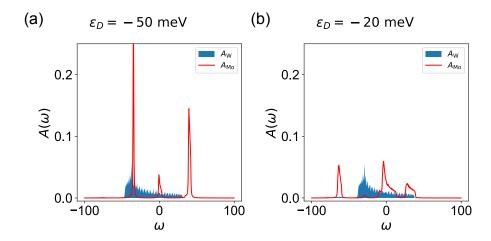


FIG. 9. The local density of states of the physical fermions with different displacement field. The parameters are chosen to be the same as in Figs. 8(c-d).

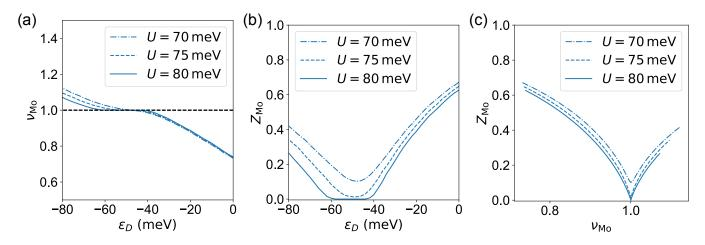


FIG. 10. (a) The filling factor of the d orbital as functions of displacement field strength with different interaction strength $U=70\,\mathrm{meV},\ U=75\,\mathrm{meV}$ and $U=80\,\mathrm{meV}$. (b) The quasiparticle weight of the d orbital with different interaction strength. (c) The d orbital quasiparticle weight as functions of its filling factor with different interaction strength. The total filling factor is set to $\nu=1.4$.

the on-site interaction U.

Appendix E: Orbital-selective Mott transition via strong interaction

In the main text, we discussed the orbital-selective Mott phase obtained by reducing the conduction electron density. The orbital-selective Mott phase transition can be achieved by increasing the interaction strength as well. The d orbital filling factor at the same total filling factor $\nu=1.4$ with different interaction strength up to $U=80\,\mathrm{meV}$ is shown in Fig. 10(a). It is obvious that the "plateau," in which the heavy Fermi liquid state is situated, broadens as the interaction becomes stronger. However, the width of the "plateau" along the ε_D axis is still much smaller than the on-site interaction U. The quasiparticle weight of the d orbital, shown in Figs. 10(b) and 10(c), also exhibits the orbital-selective Mott phase at total filling $\nu=1.4$ when the interaction is increase to $U=80\,\mathrm{meV}$.

Appendix F: Phase diagram in experiment

In Fig. 11 we show the experimentally observed electrostatics phase diagram adapted from Ref. [3]. The two axes of this phase diagram are the total filling factor ν and the displacement field strength E, which effectively is a linear

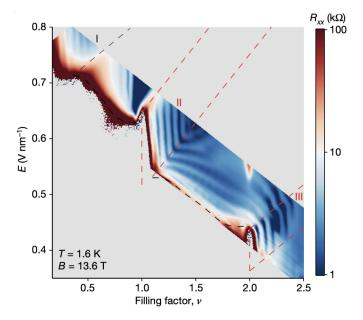


FIG. 11. The experimental electrostatics phase diagram in the parameter space (ν, E) , in which ν is the total electron density, and E is the electric field strength. The heavy Fermi liquid regime with filling factor $\nu = 1 + x$ is labeled by "II". This figure is reproduced from Fig. 2(a) in Ref. [3].

function to its corresponding potential ε_D . The measurement is performed with the presence of an out-of-plane magnetic field. Therefore, quantum oscillation patterns can be observed when ν is varied. The Landau fans are vertical within the regions labeled by red dashed lines, which indicate the Fermi surfaces are almost unchanged by the displacement field when ν is fixed. This phenomenon indeed corresponds to the plateaus in the filling factors of the two orbitals in Fig. 3(b), marking the formation of the heavy Fermi liquid state. We also note that the shape of this region in the (ν, E) phase diagram is qualitatively identical to Fig. 3(a). This phase diagram also shows that, by controlling the total filling factor ν and the displacement field E together, both ν_{Mo} and ν_{W} can be indirectly tuned in experiment.